



Citation for published version:

Vadas, SL, Figueiredo, C, Becker, E, Huber, JD, Themens, DR, Hindley, N, Mrak, S, Galkin, I & Bossert, K 2023, 'Traveling ionospheric disturbances induced by the secondary gravity waves from the Tonga eruption on 15 January 2022: Modeling with MESORAC-HIAMCM-SAMI3 and comparison with GPS/TEC and ionosonde data', *Journal of Geophysical Research: Space Physics*, vol. 128, no. 6, e2023JA031408.
<https://doi.org/10.1029/2023JA031408>

DOI:

[10.1029/2023JA031408](https://doi.org/10.1029/2023JA031408)

Publication date:

2023

Document Version

Publisher's PDF, also known as Version of record

[Link to publication](#)

© 2023. American Geophysical Union. All Rights Reserved.

University of Bath

Alternative formats

If you require this document in an alternative format, please contact:
openaccess@bath.ac.uk

General rights

Copyright and moral rights for the publications made accessible in the public portal are retained by the authors and/or other copyright owners and it is a condition of accessing publications that users recognise and abide by the legal requirements associated with these rights.

Take down policy

If you believe that this document breaches copyright please contact us providing details, and we will remove access to the work immediately and investigate your claim.

JGR Space Physics

RESEARCH ARTICLE

10.1029/2023JA031408

Key Points:

- Globally-propagating concentric TIDs are induced by secondary GWs from the Tonga eruption with $c_H = 100\text{--}750$ m/s and $\tau_r = 30$ min to 3 hr
- The fastest LSTIDs from Tonga in the far field are eliminated when detrending SAMI3 and GPS/TEC data with a 30 min window
- The fastest modeled LSTIDs from Tonga reach the US and South America at 8:30-9:00 UT with $c_H = 600$ m/s, in good agreement with data

Supporting Information:

Supporting Information may be found in the online version of this article.

Correspondence to:

S. L. Vadas,
vasha@nwr.com

Citation:

Vadas, S. L., Figueiredo, C., Becker, E., Huba, J. D., Themens, D. R., Hindley, N. P., et al. (2023). Traveling ionospheric disturbances induced by the secondary gravity waves from the Tonga eruption on 15 January 2022: Modeling with MESORAC-HIAMCM-SAMI3 and comparison with GPS/TEC and ionosonde data. *Journal of Geophysical Research: Space Physics*, 128, e2023JA031408. <https://doi.org/10.1029/2023JA031408>

Received 17 FEB 2023

Accepted 29 APR 2023

Author Contributions:

Conceptualization: Sharon L. Vadas

Data curation: Sharon L. Vadas

Formal analysis: Sharon L. Vadas, Cosme Figueiredo, David R. Themens, Neil P. Hindley, Sebastijan Mrak

Funding acquisition: Sharon L. Vadas

Investigation: Sharon L. Vadas, Cosme Figueiredo, David R. Themens, Neil P. Hindley

Methodology: Sharon L. Vadas, Cosme Figueiredo, Erich Becker, J. D. Huba, David R. Themens

Traveling Ionospheric Disturbances Induced by the Secondary Gravity Waves From the Tonga Eruption on 15 January 2022: Modeling With MESORAC-HIAMCM-SAMI3 and Comparison With GPS/TEC and Ionosonde Data

Sharon L. Vadas¹ , Cosme Figueiredo² , Erich Becker¹ , J. D. Huba³ , David R. Themens⁴ , Neil P. Hindley⁵ , Sebastijan Mrak⁶ , Ivan Galkin⁷ , and Katrina Bossert^{8,9} 

¹Northwest Research Associates, Boulder, CO, USA, ²National Institute for Space Research, INPE, São Paulo, Brazil, ³Syntek Technologies, Fairfax, VA, USA, ⁴University of Birmingham, Birmingham, UK, ⁵Centre for Space, Atmospheric and Oceanic Science, University of Bath, Bath, UK, ⁶Space Weather Research, Technology and Education Center, University of Colorado, Boulder, CO, USA, ⁷Space Science Laboratory, Department of Physics and Applied Physics, University of Massachusetts Lowell, Lowell, MA, USA, ⁸School of Earth and Space Exploration, Arizona State University, Tempe, AZ, USA, ⁹School of Mathematical and Statistical Sciences, Arizona State University, Tempe, AZ, USA

Abstract We simulate the gravity waves (GWs) and traveling ionospheric disturbances (TIDs) created by the Hunga Tonga-Hunga Ha'apai (hereafter “Tonga”) volcanic eruption on 15 January 2022 at ~04:15 UT. We calculate the primary GWs and forces/heatings generated where they dissipate with MESORAC, the secondary GWs with HIAMCM, and the TIDs with SAMI3. We find that medium and large-scale TIDs (MSTIDs and LSTIDs) are induced by the secondary GWs, with horizontal phase speeds $c_H \approx 100\text{--}750$ m/s, horizontal wavelengths $\lambda_H \approx 600\text{--}6,000$ km, and ground-based periods $\tau_r \approx 30$ min to 3 hr. The LSTID amplitudes over New Zealand are $\approx 2\text{--}3$ TECU, but decrease sharply $\approx 5,000$ km from Tonga. The LSTID amplitudes are extremely small over Australia and South Africa because body forces create highly asymmetric GW fields and the GWs propagate perpendicular to the magnetic field there. We analyze the TIDs from SAMI3 and find that a 30 min detrend window eliminates the fastest far-field LSTIDs. We analyze the GPS/TEC via detrending with 2–3 hr windows, and find that the fastest LSTIDs reach the US and South America at ~8:30–9:00 UT with $c_H \approx 680$ m/s, $\lambda_H \approx 3,400$ km, and $\tau_r \approx 83$ min, in good agreement with model results. We find good agreement between modeled and observed TIDs over New Zealand, Australia, Hawaii, Japan and Norway. The observed F-peak height, hmF2, drops by $\approx 110\text{--}140$ km over the western US with a 2.8 hr periodicity from 8:00 to 13:00 UT. We show that the Lamb waves (LWs) observed by AIRS with $\lambda_H = 380$ km have amplitudes that are $\approx 2.3\%$ that of the primary GWs at $z \approx 110$ km. We conclude that the observed TIDs can be fully explained by secondary GWs rather than by “leaked” LWs.

Plain Language Summary Gravity waves (GWs) are created by various processes, such as volcanic eruptions. A breaking GW imparts momentum and energy to the atmosphere, which creates secondary GWs. Traveling ionospheric disturbances (TIDs) are created by GWs through collisions between neutral and ion molecules. We simulate the GWs and TIDs created by the Tonga eruption on 15 January 2022. We find that medium and large-scale TIDs (MSTIDs and LSTIDs) are induced by the secondary GWs. These TIDs propagate globally, and have speeds of 100–750 m/s and horizontal scales of hundreds to thousands of km. The fastest TIDs reach the United States and South America at ~8:30–9:00 UT; these TIDs have large scales and large periods, in agreement with observations. These LSTIDs can only be seen if they are not “detrended out” when processing the ionospheric data. Previous studies eliminated these LSTIDs by restricting their detrend windows, and then incorrectly suggested that Lamb waves were responsible for the TIDs they observed. Using longer detrend windows, we find good agreement between the modeled and observed TIDs. We find that the observed TIDs can be fully explained by secondary GWs, rather than by the leakage of Lamb waves into GWs.

1. Introduction

On 15 January 2022, a submarine volcano erupted many times over several hours beginning at ~04:15 UT at Hunga Tonga-Hunga Ha'apai (hereafter “Tonga”) at 20.54°S and 175.38°W (Astafyeva et al., 2022), thereby creating atmospheric gravity waves (GWs) and Lamb waves (LWs) that propagated into the stratosphere globally

Project Administration: Sharon L. Vadas
Resources: Sharon L. Vadas, Cosme Figueiredo, Erich Becker, J. D. Huba, David R. Themens, Neil P. Hindley, Ivan Galkin
Software: Sharon L. Vadas, Erich Becker, J. D. Huba, David R. Themens, Ivan Galkin
Supervision: Sharon L. Vadas
Validation: Sharon L. Vadas
Visualization: Sharon L. Vadas, Cosme Figueiredo, Neil P. Hindley, Sebastijan Mrak
Writing – original draft: Sharon L. Vadas
Writing – review & editing: Sharon L. Vadas, Cosme Figueiredo, Erich Becker, J. D. Huba, David R. Themens, Neil P. Hindley, Sebastijan Mrak, Ivan Galkin, Katrina Bossert

(e.g., Wright et al., 2022). LWs were observed propagating globally near the Earth's surface for up to 6–7 days after the eruption (Amores et al., 2022; Heki, 2022; Matoza et al., 2022; Otsuka, 2022). At higher altitudes, medium-large to large-scale GWs from Tonga were observed propagating globally in the thermosphere using zonal wind measurements from the Michelson Interferometer for Global High-resolution Thermospheric Imaging (MIGHTI) on The National Aeronautics and Space Administration (NASA) Ionospheric Connection Explorer (ICON) (Harding et al., 2022; Vadas, Becker, Figueiredo, et al., 2023). Additionally, TIDs from Tonga were observed propagating locally and globally in the F region ionosphere from ground-based vertical total electron content (vTEC) data (Heki, 2022; Lin et al., 2022; Themens et al., 2022; Verhulst et al., 2022; Wright et al., 2022; Zhang et al., 2022). Due to its scope and scale, the Tonga eruption was a unique and extremely important event because it enabled a natural laboratory for the study of waves in the atmosphere and ionosphere.

Wright et al. (2022) observed 3 TIDs from Tonga over New Zealand with (a) $c_H \approx 667$ m/s and $\lambda_H \approx 1,000$ km; (b) $c_H \approx 414$ m/s and $\lambda_H \approx 700$ km; and (c) $c_H \approx 343$ m/s and $\lambda_H \approx 400$ km, where c_H is the ground-based horizontal phase speed and λ_H is the horizontal wavelength. Although they also observed TIDs (b) and (c) (as well as TID (d) with $c_H \approx 311$ m/s) over North America, they did not observe TID (a) there. Although the GWs that induced TIDs (c) and (d) (through ion-neutral collisions) could have propagated directly from the Tonga eruption (as primary GWs) to North America in principle, the GWs that induced TIDs (a) and (b) could not have (i.e., could not be primary GWs from the eruption) because c_H was too large (Extended Data Figure 6 of Wright et al., 2022); this is because the maximum intrinsic horizontal phase speed, c_{IH} , a GW can have at $z < 140$ km is $c_{IH} \leq 0.9c_s$, where c_s is the sound speed (e.g., Vadas et al., 2019). Since $c_s \approx 310$ – 320 m/s in the lower atmosphere, the maximum speed a GW can have there is $c_{IH} \leq 280$ – 290 m/s.

Wright et al. (2022) also observed LWs in the stratosphere, which propagated 3 times around the Earth, with $c_H \approx 300$ – 320 m/s, $\lambda_H \sim 100$ – 200 km and observed period $\tau_r = \lambda_H/c_s \sim 5$ – 10 min [their Extended Data Figure 5). Here, a LW is a special type of acoustic wave (AW) that propagates horizontally at the sound speed, has zero vertical velocity $w' = 0$, and has no vertical structure, $|\lambda_z| = \infty$ (Lamb, 1932). Note that a LW is not an acoustic-gravity wave, as suggested by Matoza et al. (2022). Even though a LW only propagates horizontally, its amplitude increases exponentially in altitude as

$$e^{\alpha z} = e^{z/(2H)} \exp\left(\frac{(\gamma - 2)z}{2\gamma H}\right) \quad (1)$$

(from Equations A10 and A22), where α is a constant determined as part of the LW solution, H is the (neutral) density scale height, and $\gamma = C_p/C_v$ is the ratio of the specific heat at constant pressure (C_p) to the specific heat at constant volume (C_v). However, a LW's amplitude does not grow as rapidly in z as do the amplitudes of GWs and AWs (since the second term on the right-hand-side of Equation 1 is < 1). The periodic oscillation of the fluid (e.g., u') created in the lower thermosphere by a LW can force the excitation of GWs there (Nishida et al., 2014). At this altitude, c_s has increased sufficiently (because of the increasing background temperature \bar{T}) such that 300 – 320 m/s $\lesssim 0.9c_s$ there. Such a forced GW would then have the same frequency ($\omega_r = 2\pi/\tau_r$), λ_H and c_H as the LW, but with a vertical wavelength λ_z determined by the GW dispersion relation. A GW requires $\tau_{tr} > \tau_B$, where τ_{tr} is the intrinsic period and τ_B is the buoyancy period. If $\tau_{tr} = \tau_B$, an upward-propagating GW will reflect downward. Since $\tau_B \approx 9$ – 12 min in the F region, it is likely that a forced (leaked) GW with $\tau_r = 5$ – 10 min would be trapped in the lower thermosphere, limited by $c_{IH} < 0.9c_s$ from below and $\tau_{tr} > \tau_B$ from above; such GWs would not reach the F region, and would therefore not induce TIDs. Thus, only leaked LWs with $\tau_{tr} \geq 10$ – 12 min could have the potential to influence the F region ionosphere. Using $c_s = 318$ m/s, this requirement is satisfied for $\lambda_H \geq 190$ – 230 km.

Themens et al. (2022) analyzed TIDs from Tonga with $\tau_r \approx 10$ – 40 min from GPS/TEC data via detrending with a 30-min boxcar window. They observed LSTIDs L1 and L2 over New Zealand. L1 had $c_H \approx 950$ m/s, $\tau_r \approx 48$ min, and $\lambda_H > 1,600$ km at distances from Tonga, \mathcal{R} , of $\mathcal{R} \approx 1,800$ – $2,000$ km and at 5:00 UT that “slowed” significantly at greater distances and times (their Figure 3). It is unclear if this TID was induced by a Rayleigh wave or a GW since the calculated speed depended sensitively on the nearly vertical slope of the wave phases in their keogram. L2 was observed at 5:30 UT with the same λ_H and τ_r , but with $c_H \approx 555$ m/s at $\mathcal{R} \approx 1,800$ km; this wave “slowed” to $c_H \approx 390$ m/s at 6:00–6:20 UT at $\mathcal{R} \approx 2,500$ – $3,400$ km. These latter TIDs were likely induced by GWs through ion-neutral collisions since $\tau_{tr} > \tau_B$. Note that because GWs propagate horizontally and vertically simultaneously, the GW that arrived at 6:00 UT was a different GW with a slower vertical group velocity and smaller

c_H than the GW that arrived at 5:30 UT. Following L1 and L2, MSTIDs were observed for ~ 6 hr after the eruption up to distances of $\mathcal{R} \simeq 16,000$ km with $c_H \simeq 200\text{--}400$ m/s, $\lambda_H \simeq 250\text{--}500$ km and $\tau_r \simeq 10\text{--}25$ min. As a clue to the source of these waves, Themens et al. (2022) found that the LSTIDs were distributed non-symmetrically: “the fast LSTID structures are barely discernible in Australia, suggesting substantial attenuation of the waves to the West. These modes are completely absent in South Africa, which is roughly along the same propagation trajectory from the source as Australia. This suggests a substantial disinclination of the LSTID propagation to the West from the eruption. In contrast, the first and second LSTID signatures are the dominant structures seen at Hawaii to the north East...” Although they did not specifically retain TIDs with $\tau_r > 1$ hr, faint LSTIDs with $\tau_r > 1$ hr are seen in their Figure 4 over Hawaii, Japan and northern Europe. Importantly, they did not observe MSTIDs with $c_H > 400$ m/s at $\mathcal{R} > 4,000$ km.

Zhang et al. (2022) analyzed the TIDs from Tonga with $\tau_r \simeq 10\text{--}30$ min using a 30 min detrend window. They found that the TIDs (which they incorrectly called “enormous shocks”—see Sec. 3.1) had c_H up to $\simeq 700$ m/s at $\mathcal{R} \leq 4000$ km near Tonga, with amplitudes of dTEC = 3 TECU. (Here, 1 TECU = 10^{16} electrons/m².) These TIDs had $\tau_r > 12$ min, and were therefore likely induced by GWs. Further away however, the TIDs that remained after detrending had $c_H \simeq 350$ m/s. The fastest TIDs reached the western continental United States (CONUS) at $\sim 11:00\text{--}12:00$ UT with $c_H \simeq 350$ m/s, and departed off the eastern CONUS at $\sim 16:00$ UT with the same c_H and $\lambda_H \simeq 500$ km. They found that these latter waves propagated around Earth 3 times over 4 days, passing over the CONUS six times over 100 hr, with $c_H \simeq 350$ m/s, $\lambda_H \simeq 500\text{--}1000$ km and $\tau_r \simeq 10\text{--}30$ min (their Figure 4).

Heki (2022) observed TIDs from Tonga that passed over Japan at least four times. In contrast to the LW, their TIDs had a range of phase speeds which were significantly less than to greater than 300 m/s, with $\tau_r \simeq 20\text{--}60$ min and $\lambda_H \simeq 600\text{--}1,800$ km (their Figure 6). They called the TIDs with $c_H > 300$ m/s “precursor waves” (e.g., their Figure 8), and wrote “An important difference is that significant ionospheric anomalies [their Figure 6a] seem to start well before the arrival of the pressure anomaly [their Figure 3a] by the LW (Lamb Wave) passage.”

Lin et al. (2022) analyzed the TIDs with $\tau_r = 12\text{--}20$ min and $\tau_r = 30\text{--}50$ min via detrending with a Butterworth filter. They showed that the TIDs that remained after detrending had $c_H \simeq 320\text{--}390$ m/s and $\lambda_H \simeq 400\text{--}1,400$ km over New Zealand, Australia, and Japan. They also observed conjugate MSTIDs over Japan at 8:00–11:00 UT.

Because of the accidental coincidence that the globally-propagating MSTIDs that remained *after detrending* (i.e., having $\tau_r \simeq 10\text{--}50$ min at $\mathcal{R} \gg 4,000$ km) had “ballpark” horizontal phase speeds as that of the LW in the stratosphere, Lin et al. (2022) and Zhang et al. (2022) suggested that their MSTIDs were created by the leakage of stratospheric LWs into thermospheric GWs. However, as explained above, a GW with $c_H \simeq 300\text{--}320$ m/s in the thermosphere can only be created by the leakage of a LW if it has a similar value of c_H , τ_r , and λ_H , because such a GW is a *forced* wave. This is not the case here. As detailed in Section 6, the stratospheric LWs observed by the Atmospheric InfraRed Sounder (AIRS) had $\lambda_H \simeq 70\text{--}380$ km and $c_H = 318.2 \pm 5.7$ m/s (and $\tau_r \simeq 3.6\text{--}20.3$ min). However, the far-field MSTIDs observed by Lin et al. (2022) and Zhang et al. (2022) had $\lambda_H \simeq 400\text{--}2,000$ km; thus λ_H does not agree with the AIRS observations. In addition, all of the Zhang et al. (2022) and nearly all of the Lin et al. (2022) far-field MSTIDs had larger c_H than the LWs observed by AIRS. Additionally, we show in Appendix A that the LW amplitude is 2.3% that of the primary GW at the approximate leakage altitude of $z \simeq 110$ km. This tiny amplitude ratio occurs because a LW's amplitude decays exponentially in altitude relative to a GW's amplitude. Since the secondary GW amplitudes are 5–10 times smaller than the primary GW amplitudes, the LW amplitudes are 4–9 times smaller than the secondary GW amplitudes (see Appendix A). Therefore, virtually none of the far-field MSTIDs observed by Lin et al. (2022) and Zhang et al. (2022) could have been created by the leakage of LWs into the thermosphere. What then created these TIDs and GWs?

Vadas, Becker, Figueiredo, et al. (2023) recently modeled the primary and secondary GWs created by the Tonga eruption on 15 January 2022 using the Model for gravity wave SOURCE, Ray tracing and reConstruction (MESORAC) and the High Altitude Mechanistic general Circulation Model (HIAMCM). These secondary GWs were generated by the imbalances of the large-scale ambient flow which in turn were created by the transfer of momentum and energy from the dissipation of the primary GW packets. They found that although the primary GWs from Tonga were localized within $\simeq 500\text{--}600$ km of Tonga in the thermosphere, the secondary GWs propagated globally with a wide range of medium to large scales and speeds of $\lambda_H \simeq 400\text{--}7,500$ km, $c_H \simeq 100\text{--}600$ m/s, and $\tau_r \simeq 20$ min to 7 hr. They found that the fastest secondary GWs were large scale and reached the western CONUS at $\sim 8:30$ UT, with $c_H \simeq 500\text{--}600$ m/s, $\lambda_H \simeq 3,000\text{--}7,500$ km and $\tau_r \simeq 1.5\text{--}7$ hr. They conjectured that Zhang et al. (2022) and Lin et al. (2022) did not observe the LSTIDs induced by these GWs over the CONUS

because they restricted their analyses to TIDs with $\tau_r \leq 30$ min and $\tau_e \leq 50$ min, respectively. Vadas, Becker, Figueiredo, et al. (2023) also analyzed the GWs observed by MIGHTI during four consecutive passes of ICON on 15 January 2022 at 12:00–19:00 UT, and found that the observed GWs had a wide range of medium-large to large scales and phase speeds of $\lambda_H \simeq 800$ –7,500 km and $c_H \simeq 100$ –600 m/s, in excellent agreement with the modeled secondary GWs. They also found good agreement between the location, amplitudes, timing and wavelengths of the Tonga waves with the model results, provided the model GW amplitudes were increased by $\simeq 2$ and were sampled $\simeq 30$ min later than ICON-MIGHTI. They argued that this underestimation was likely because they had to limit the body forces/heatings computed by MESORAC (via adjusting the turbulent diffusion parameter in the saturation scheme) to prevent the HIAMCM Tonga run (where these body forces/heatings were added as wind and temperature tendencies) from becoming unstable. They also found good agreement between the observed and modeled tides and the onset of the sunset terminator wave. They concluded that the GWs observed by ICON-MIGHTI were secondary GWs excited by the spatially and temporally-localized body forces/heatings created by the dissipation of primary GWs from Tonga, and were therefore not thermospheric GWs forced by the leakage of stratospheric LWs.

Li et al. (2023) recently investigated the neutral density in the thermosphere at $z \sim 500$ km observed by the GRACE-FO and Swarm-C satellites after the Tonga eruption. They observed three thermospheric waves that propagated concentrically across the globe, with two of them reaching the antipode. These waves had $c_H \simeq 452$, 304, and 207 m/s. The fastest wave with $c_H \simeq 452$ m/s had a very large amplitude of $\simeq 150\%$ above the background density, and was observed to reach the antipode just after 13:30 UT.

Huba et al. (2023) coupled the Sami3 is Also a Model of the Ionosphere (SAMI3) with the HIAMCM results. They found that the Tonga event created a “super” equatorial plasma bubble that extended $\sim 30^\circ$ in longitude and up to 500 km in altitude, and had a density depletion of three orders of magnitude.

In this study, we analyze the TIDs induced by the secondary GWs from Tonga using the MESORAC, HIAMCM, and SAMI3 models, and compare them with GPS/TEC and ionosonde observations. We review the methodology used to generate the GWs and TIDs from Tonga in Section 2. Section 3 analyzes the TIDs induced by these secondary GWs using various detrend windows, and compares them with vTEC TIDs worldwide. Section 4 compares the modeled TIDs with those observed over the CONUS and South America from vTEC using various detrend windows. Section 5 compares the model results with ionosonde data over the CONUS. Section 6 determines the characteristics of the LWs observed by AIRS. Our conclusions are contained in Section 7. Appendix A derives the LW solution.

2. Modeling the GWs and TIDs From Tonga

2.1. Modeling the Primary GWs From Tonga Using MESORAC

MESORAC calculates the primary GWs generated by spatially and temporally-localized updrafts (vertical accelerations) of air in the stratosphere and mesosphere using the analytical Fourier-Laplace fully-compressible solutions (Vadas, 2013). The locations and diameters of the updrafts are determined by analyzing the cloud-top temperatures of weather satellite data. The primary GWs radiate away from the updrafts as concentric rings (Vadas, Yue, et al., 2009; Vadas et al., 2012). MESORAC ray traces these GWs forward in time (including their phases from the Fourier-Laplace solutions), and reconstructs the primary GW field at higher altitudes using the dissipative GW polarization and dispersion relations (Vadas & Fritts, 2005, 2009). Wave dissipation in MESORAC is due to molecular diffusion and turbulent diffusion from saturation. The body forces and heatings created by the dissipation of the primary GWs are calculated as functions of space and time (Vadas, 2013). These ambient-flow effects are then added to the momentum and thermodynamic equations of the HIAMCM to simulate the secondary GWs. (In this paper, we use the term “secondary GWs” to refer to the GWs generated by the atmosphere’s response to the temporally and spatially-localized deposition of momentum and energy that occurs from the dissipation of the primary GWs from Tonga.)

On 15 January 2022, the first of many updrafts from the Tonga eruption occurred at $\sim 4:15$ UT (Astafyeva et al., 2022). These updrafts were observed by NOAA’s Geostationary Operational Environmental Satellite (GOES)-17. Here, we only include the primary GWs generated by the updrafts from 4:15 to 5:50 UT, not by the updrafts associated with the deep convection that occurred many hours later from the large injection of water into the atmosphere (e.g., Wright et al., 2022]. The background atmosphere we use for the ray tracing

is the “base” HIAMCM simulation on 15 January 2022 without the Tonga eruption using horizontal scales of $\lambda_H > 2,000$ km. Further details of MESORAC's calculation of the primary GWs from Tonga are given in Vadas, Becker, Figueiredo, et al. (2023).

2.2. Modeling the Secondary GWs From Tonga Using the HIAMCM

The HIAMCM is a high-resolution, whole-atmosphere model for the neutral dynamics which simulates GWs explicitly. It employs a spectral dynamical core with a terrain-following hybrid vertical coordinate, which is extended by consistent thermodynamics in the thermosphere, as well a correction for nonhydrostatic dynamics. The version we employ here uses a triangular spectral truncation at a total wavenumber of 256. This corresponds to a horizontal grid spacing of ~ 52 km. Our current version has a model top at 4×10^{-9} hPa and includes 280 full levels, with altitude-dependent vertical resolution. For an exospheric temperature of $\bar{T} \sim 950$ K, the model top is at $z \sim 450$ km. The effective resolution of the HIAMCM is $\lambda_H \simeq 200$ km. Resolved GWs are dissipated predominantly by macro-turbulent diffusion at $z < 200$ km using the Smagorinsky-type diffusion scheme, and by molecular diffusion at higher altitudes. Topography and a simple ocean model, as well as radiative transfer, boundary layer processes, and the tropospheric moisture cycle are fully taken into account. In order to allow for the simulation of observed events, we nudge the large scales of the HIAMCM to Modern-Era Retrospective analysis for Research and Applications, Version 2 (MERRA-2) reanalysis in the troposphere and stratosphere. A simple ion drag parameterization is included. Further details of the HIAMCM are given in Becker and Vadas (2020) and (Becker, Vadas, et al., 2022, Becker, Goncharenko, et al., 2022, see also references therein).

We perform two HIAMCM simulations here. The first, the “base run”, is the HIAMCM run on 15 January 2022 without the inputs from MESORAC. The second, the “Tonga run”, is the HIAMCM run on 15 January 2022 with the inputs from MESORAC. Further details of HIAMCM's calculation of the secondary GWs from Tonga are given in Vadas, Becker, Figueiredo, et al. (2023). Note that the HIAMCM runs do not include geomagnetic forcing.

2.3. Modeling the MSTIDs and LSTIDs From Tonga Using SAMI3

SAMI3 is a seamless, global, three-dimensional, physics-based model of the ionosphere/plasmasphere system. It is based on the original SAMI2 model (Huba et al., 2000). SAMI3 models the plasma and chemical evolution of seven ion species (H^+ , He^+ , N^+ , O^+ , N_2^+ , NO^+ , and O_2^+). The temperature equation is solved for three ion species (H^+ , He^+ , and O^+) and for the electrons. Further details of the model have been discussed in previous papers (e.g., Huba & Joyce, 2010; Huba & Liu, 2020; Huba et al., 2023). We note that a feature of the SAMI3 model used in this study is the implementation of a fourth order flux-corrected transport scheme for $E \times B$ transport perpendicular to the magnetic field. The partial donor cell method (Hain, 1987; Huba, 2003) is used which reduces numerical diffusion and allows steep density gradients to develop that occur on the sides of equatorial plasma bubbles (EPBs). Further details of SAMI's calculation of the TIDs from Tonga are given in Huba et al. (2023). To better-resolve the MSTIDs induced by the GWs, the SAMI3 is forced with a 5 min time cadence of HIAMCM data, and the output cadence of the SAMI3 data is 5 min.

We note that SAMI3 does not generate the secondary GWs from Tonga. Instead, the HIAMCM generates the secondary GWs and large-scale wind changes from Tonga, then SAMI3 calculates how these GWs and large-scale wind changes affect the ionosphere (including the TIDs generated from these GWs) through the modification of the neutral wind. Note that these SAMI3 runs do not include geomagnetic forcing.

3. Secondary GWs and TIDs

3.1. Modeled Secondary GWs and TIDs

Figure 1 shows the temperature response, $\Delta T = T - T_{\text{base}}$, computed from the HIAMCM Tonga run minus the base run at $z = 280$ km at various times from 6:00 to 22:00 UT on 15 January 2022. Secondary GWs with concentric ring structure radiate away from Tonga with $c_H \simeq 100\text{--}750$ m/s. Those with $c_H \simeq 700\text{--}750$ m/s are only observed close to Tonga: $R \leq 5000$ km. For each snapshot, λ_H increases rapidly with radius R from Tonga, as expected for GWs excited by a point source (e.g., Yue et al., 2009; Vadas, Yue, et al., 2009). The fastest GWs are large-scale GWs (defined as $\lambda_H \geq 1,000$ km) with $c_H \simeq 600\text{--}750$ m/s, and propagate in all directions except west and east. This is why the amplitudes of the large-scale GWs over Australia, South Africa and Ecuador are very small. This

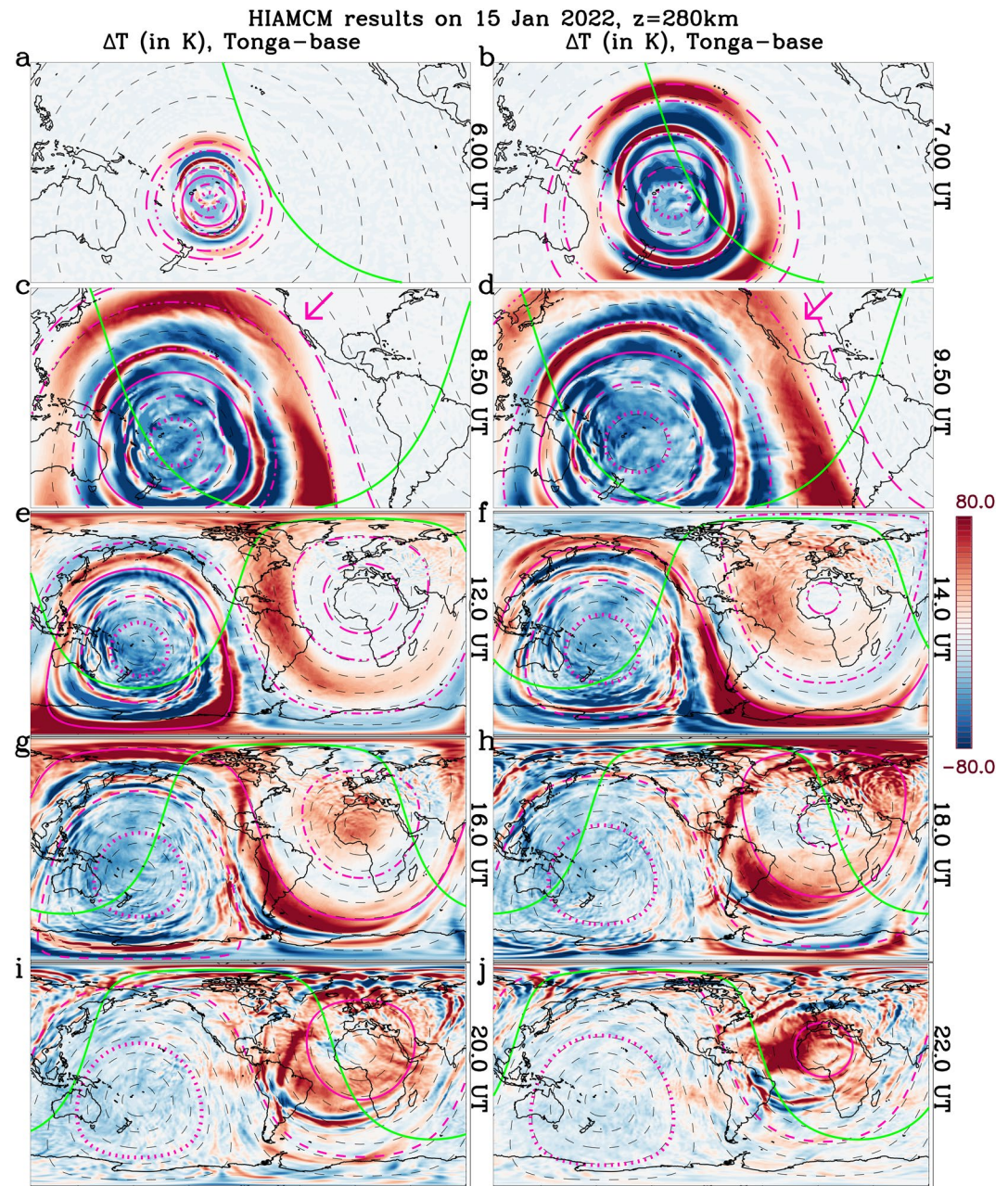


Figure 1. HIAMCM ΔT (in K) at $z = 280$ km computed from the Tonga run minus the base run on 15 January 2022 at 6:00, 7:00, 8:30, 9:30, 12:00, 14:00, 16:00, 18:00, 20:00, and 22:00 UT, as labeled. The black dash lines show equi-distances from Tonga in 1,500 km intervals. Pink dot, dash, solid, dash-dot, dash-dot-dot-dot, and long dash lines show the locations of thermospheric GWs that originated above Tonga at 5:00 UT with $c_H = 100, 200, 300, 400, 600,$ and 700 m/s, respectively. The green solid lines show the solar terminator. The colors are oversaturated to emphasize the waves. Pink arrows point to the fastest secondary GWs reaching (c) and propagating over (d) the CONUS.

asymmetry in the secondary GW radiation pattern is a standard feature of GWs excited by a horizontal body force, whereby none of the GWs propagate perpendicular to the force direction (Vadas et al., 2003, 2018). Instead, the secondary GWs propagate mainly within four cone-shaped wave “beams” which are oriented forward/upward, forward/downward, backward/upward and backward/downward with respect to the force direction. Because of the asymmetry shown in Figure 1, we infer that the body forces are directed meridionally; this is in fact correct (Figure 4 from Vadas, Becker, Figueiredo, et al., 2023), and is due to the strong filtering of the primary GWs during the eruptions (17:19–18:00 local time (LT)) by the background meridional wind in the thermosphere.

In the “near-field”, the first secondary GWs reach New Zealand at $\sim 6:00$ UT with fast speeds of $c_H \simeq 700$ m/s. By 7:00 UT, the amplitudes over New Zealand are very large: $\Delta T \simeq 100\text{--}200$ K. On the other hand, the first secondary GWs reach Australia at $\sim 7:30$ UT with much slower speeds of $c_H \simeq 400$ m/s and much weaker amplitudes. By 8:30 UT, the amplitudes over Australia are $\Delta T \simeq 30$ K. Both the timing and phase speeds at these sites agree well with observations (e.g., Themens et al., 2022; Zhang et al., 2022).

In the “far-field”, the first secondary GWs reach the western CONUS at $\sim 8:30\text{--}9:00$ UT and have $\lambda_H \simeq 3,000\text{--}4,000$ km and $c_H \simeq 600$ m/s. Using $\tau_r = \lambda_H/c_H$, these GWs have large periods of $\tau_r \simeq 1.3\text{--}1.9$ hr. This arrival time is 2.5 hr earlier than the slower waves reported by Zhang et al. (2022), and is due to the fact that they removed TIDs with $\tau_r > 30$ min (see below). The first secondary GWs reach the southern part of South America at $\sim 9:00$ UT with the same wave parameters as for the western CONUS. Note that this latter GW packet propagated southeastward from Tonga over the southern high latitude region before reaching South America. The first secondary GWs reach Hawaii by 7:00 UT ($c_H \simeq 700$ m/s, $\lambda_H \simeq 2,200\text{--}2,400$ km, $\tau_r \simeq 55$ min), Japan at 8:30 UT ($c_H \simeq 600\text{--}650$ m/s, $\lambda_H \simeq 3,000\text{--}3,500$ km, and $\tau_r \simeq 1.3\text{--}1.6$ hr), and northern Europe at 12:00 UT ($c_H \simeq 600$ m/s, $\lambda_H \simeq 3,000\text{--}4,000$ km, and $\tau_r \simeq 1.3\text{--}1.9$ hr). Note that the GW amplitudes over northern Europe are much weaker than those over Japan and Hawaii, presumably due to wave dispersion, wave dissipation and geometric attenuation. Finally, the first secondary GWs reach South Africa at 13:00 UT with the same wave parameters as the first GWs over the CONUS, South America and northern Europe.

The fact that the fastest GWs at these sites are large-scale and have large periods is not surprising, and can be understood by examining the isothermal, windless expressions for GWs excited by a point source (Equations 4, 8 and 13 of Vadas & Azeem, 2021):

$$\tau_{Ir} = \tau_B \left[\left(\frac{\mathcal{R}}{\Delta z} \right)^2 + 1 \right]^{1/2}, \quad (2)$$

$$\lambda_H \simeq |c_{gz}| \tau_B \left[\left(\frac{\mathcal{R}}{\Delta z} \right)^2 + 1 \right], \quad (3)$$

$$c_{IH} = |c_{gz}| \left[\left(\frac{\mathcal{R}}{\Delta z} \right)^2 + 1 \right]^{1/2}, \quad (4)$$

where $\Delta z = z_{\text{obs}} - z_{\text{source}}$, z_{source} is the altitude of the point source, z_{obs} is the observation altitude, \mathcal{R} is the radius from the source (in the horizontal plane at z_{obs}), c_{IH} is the intrinsic horizontal phase speed, and c_{gz} is the vertical group velocity. At a given time t , all GWs that reach the height z_{obs} have the same value of c_{gz} . At that snapshot time, τ_{Ir} and c_{IH} increase linearly with \mathcal{R} and λ_H increases quadratically with \mathcal{R} in the far-field (i.e., where $\mathcal{R} \gg \Delta z$). From Equations 2 and 4, τ_{Ir} is proportional to c_{IH} at this given time t :

$$\tau_{Ir} = \frac{\tau_B}{|c_{gz}|} c_{IH}. \quad (5)$$

Thus, at a given time t , GWs at the largest radii \mathcal{R} are the fastest, and have the largest periods τ_{Ir} . Therefore, analysis techniques that remove waves with $\tau_r > 30\text{--}50$ min cannot observe the fastest waves from Tonga at large \mathcal{R} .

Figure 1 also shows that the medium-scale GWs (defined as $100 \leq \lambda_H < 1,000$ km) reach the western CONUS at $\sim 12:00$ UT, in good agreement with observations (Zhang et al., 2022). They also reach Australia at $\sim 8:30$ UT, South America at $\sim 12:00\text{--}13:00$ UT, South Africa at $\sim 17:00\text{--}18:00$ UT, and Japan at $\sim 11:00\text{--}12:00$ UT.

Figure 2 shows the TEC response, ΔTEC , computed from the SAMI3 Tonga run minus the base run on 15 January 2022 at 5:30, 7:00, 10:00, 12:00, and 18:00 UT. Here, the TEC from both runs have been detrended by subtracting a 30 min (left column) and 3 hr (right column) running mean in order to see the TIDs with $\tau_r \leq 30$ min and $\tau_r \leq 3$ hr, respectively. Concentric rings of TIDs radiate away from Tonga. In the near-field, the LSTIDs induced by the fastest secondary GWs reach New Zealand at $\sim 5:30$ UT with $c_H \simeq 750$ m/s and enormous amplitudes of $\simeq 2\text{--}3$ TECU. Remarkably, these speeds and amplitudes agree very well with $v\text{TEC}$ observations (Zhang et al., 2022); however, these LSTIDs are not “shock waves” as reported by that work, but are LSTIDs induced by large-scale secondary GWs through ion-neutral collisions.

In the far-field, the LSTIDs reach the CONUS and South America at $\sim 8:30$ and 9:00 UT, respectively. While the fastest LSTIDs with $c_H \simeq 600$ m/s are seen over the CONUS and South America at 10:00 UT when the 3 hr

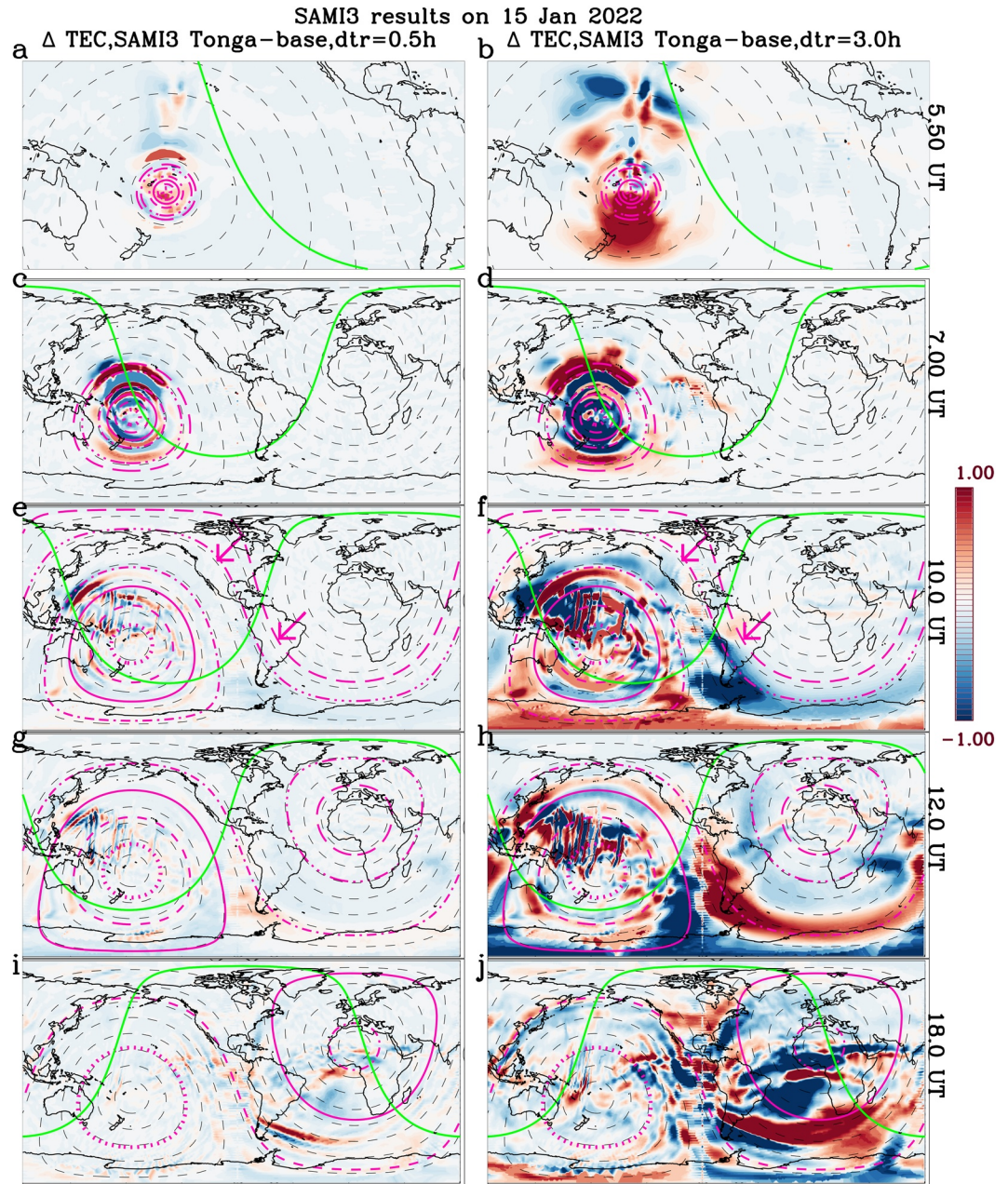


Figure 2. SAMI3 Δ TEC (in TECU) for the Tonga run minus the base run on 15 January 2022 at 5:30, 7:00, 10:00, 12:00, and 18:00 UT in rows 1–5, respectively. The TEC is detrended with a window of 30 min and 3 hr in the left and right columns, respectively. The black dash lines show equi-distances from Tonga in 1500 km intervals. Pink dot, dash, solid, dash-dot, dash-dot-dot-dot, and long dash lines show the locations of thermospheric GWs that originated above Tonga at 5:00 UT with $c_H = 100, 200, 300, 400, 600,$ and 700 m/s, respectively. The green solid lines show the solar terminator. The colors are oversaturated to emphasize the waves. Pink arrows in (e–f) show the LSTIDs induced by the fastest secondary GWs propagating over the western CONUS and South America; although these LSTIDs have significant amplitudes for the detrend window of 3 hr (f), their amplitudes are negligible for the detrend window of 30 min (e).

detrend window is applied (pink arrows in Figure 2f), they are not seen over the CONUS and South America when the 30 min detrend window is applied (pink arrows in Figure 2e); this is because these TIDs have $\tau_r \approx 1.3$ – 1.9 hr, which are effectively eliminated (detrended out) when using a 30 min detrend window. This is why Zhang et al. (2022) did not detect these fast LSTIDs over the CONUS. Note that the amplitudes of the LSTIDs over the CONUS and South America are ≈ 0.4 and ≈ 0.8 TECU, respectively, using a 3 hr detrend window.

Figure 2 shows that the TID distribution is horizontally asymmetric, similar to that of the secondary GW distribution shown in Figure 1, although the horizontal asymmetry of the TID distribution is enhanced over that of the neutrals. This enhancement occurs because \mathbf{B} is approximately northward near Tonga, and ion-neutral collisions are ineffective at creating TIDs when the GW propagation direction is perpendicular to \mathbf{B} , that is, when $\mathbf{v} \cdot \mathbf{B} \approx 0$ (e.g., Nicolls et al., 2014; Appendix A). An important result from Figure 2 is that the LSTIDs with $c_H \approx 600\text{--}750$ m/s have extremely small amplitudes over Australia and South Africa, regardless of the detrend window; this agrees well with νTEC observations (Themens et al., 2022).

It is purely coincidental that the main direction of the radiated secondary GWs is approximately aligned with \mathbf{B} . If the background wind in the thermosphere had been in the zonal direction (e.g., if the eruption had occurred 3–6 hr earlier or later), then the body forces would have been in the zonal direction. These forces would have predominantly created zonally-propagating secondary GWs, which would have induced TIDs with much smaller amplitudes in Figure 2 due to the smaller $\mathbf{v} \cdot \mathbf{B}$ values.

Figure 3a shows a keogram of the vertical wind response, Δw , for the HIAMCM Tonga run minus the base run at $z = 280$ km on 15 January as functions of time and distance along the great circle from Tonga to Fredericton, Canada (293°E and 46°N). The secondary GWs span a wide range of scales: $\lambda_H \approx 400\text{--}6,000$ km, $c_H \approx 100\text{--}750$ m/s, and $\tau_r \approx 20$ min to 4 hr. These GWs have somewhat higher phase speeds than those seen in the keogram of the meridional velocity response (Figure 7 of Vadas, Becker, Figueiredo, et al., 2023] because the vertical wind spectrum emphasizes the higher-frequency portion of the secondary GW spectrum via the GW polarization relations (e.g., Vadas, 2013]. The fastest GWs reach $\mathcal{R} \approx 9,000\text{--}13,000$ km at $\sim 8:00\text{--}10:00$ UT with $c_H \approx 500\text{--}600$ m/s, $\lambda_H \approx 3,000\text{--}4,000$ km, and $\tau_r \approx 1.3\text{--}2.2$ hr. The slower medium-scale GWs reach $\mathcal{R} \approx 9,000\text{--}13,000$ km at $\sim 12:00$ UT to at least $22:00$ UT with $c_H \approx 200\text{--}400$ m/s, $\lambda_H \approx 400\text{--}1,000$ km, and $\tau_r \approx 20$ min to 1.5 hr. This agrees with νTEC observations of TIDs over Japan at $\sim 12:00$ UT, for which $\tau_r \approx 120$ min, $c_H \approx 300$ m/s, and $\lambda_H \approx 800\text{--}1,000$ km (Heki, 2022, their Figure 5a). Note that the medium-scale GWs with the largest amplitudes over the CONUS have $c_H \approx 200\text{--}300$ m/s in Figure 3a.

Figure 3b shows a keogram of the dTEC response, ΔTEC , for the SAMI3 Tonga run minus the base run along the same great circle as in Figure 3a. Here we use a detrend window of 1 hr. TIDs with $c_H \approx 100\text{--}750$ m/s, $\lambda_H \approx 600\text{--}6,000$ km, and $\tau_r \approx 30$ min to 3 hr are seen. The amplitudes of the TIDs induced by the secondary GWs with $c_H \approx 300\text{--}750$ m/s are very large near Tonga, $\approx 2\text{--}3$ TECU, decrease sharply at $\mathcal{R} \approx 5,500$ km, then recover moderately at $\mathcal{R} \geq 8,000$ km. The sharp reduction at $\mathcal{R} \approx 5,500$ km coincides with the location of the magnetic equator ($\approx 10^\circ\text{N}$), and occurs because the GWs propagate approximately perpendicular to \mathbf{B} there: $\mathbf{v} \cdot \mathbf{B} \approx 0$. A similar result was seen for the GWs from the Tohoku earthquake, for which the southeastward TIDs disappeared at the magnetic equator (Huba et al., 2015). The result that the induced TIDs have severely-reduced amplitudes at $\mathcal{R} \approx 5,500$ km agrees well with νTEC observations (Figure 2 of Themens et al. (2022) and Figure 3 of Zhang et al. (2022)). At $\mathcal{R} > 8,000$ km (corresponding to $\approx 25^\circ\text{N}$), the TID amplitudes increase moderately to $\approx 0.2\text{--}0.4$ TECU in Figure 3b, in good agreement with observations (Themens et al., 2022; Zhang et al., 2022).

Figure 3c shows a keogram of the average dTEC response, ΔTEC , for the SAMI3 Tonga run minus the base run as functions of time and distance from Tonga. At each \mathcal{R} , we average every 2° in azimuth from 0 to 360° around Tonga. A 1 hr detrend window is applied before averaging. The average TID amplitudes decrease severely at $\mathcal{R} \approx 5,000\text{--}7,000$ km because of the varying location of the magnetic equator with azimuth around Tonga. Note that at $\mathcal{R} \geq 8,000$ km, the average TID amplitudes increase moderately, and are largest for $c_H \approx 200\text{--}400$ m/s.

3.2. Comparison of the Modeled and Observed TIDs at Stations Worldwide

Figure 4 shows keograms of the vertical wind, Δw , for the HIAMCM Tonga run minus the base run at $z = 280$ km on 15 January as functions of time and distance from Tonga along great circles to New Zealand, Australia, Hawaii, Japan, Fredericton Canada, South Africa and Tromsø Norway. We overlay the horizontal phase speeds for outbound and inbound thermospheric GWs that originated above Tonga at $5:00$ UT with $c_H = 100\text{--}700$ m/s. While the fastest GWs propagate above New Zealand and Hawaii with $c_H \approx 500\text{--}750$ m/s, the fastest GWs above Australia only have $c_H \leq 400$ m/s, in agreement with observations (Themens et al., 2022); this result is due to the asymmetry of the radiated secondary GWs, as discussed above. It appears that “inbound” GWs (with negative slopes) might be visible toward the end of 15 January over Hawaii, Japan and possibly New Zealand and Australia. However, we show in Section 3.3 that only the GWs over Japan may be inbound GWs from Tonga.

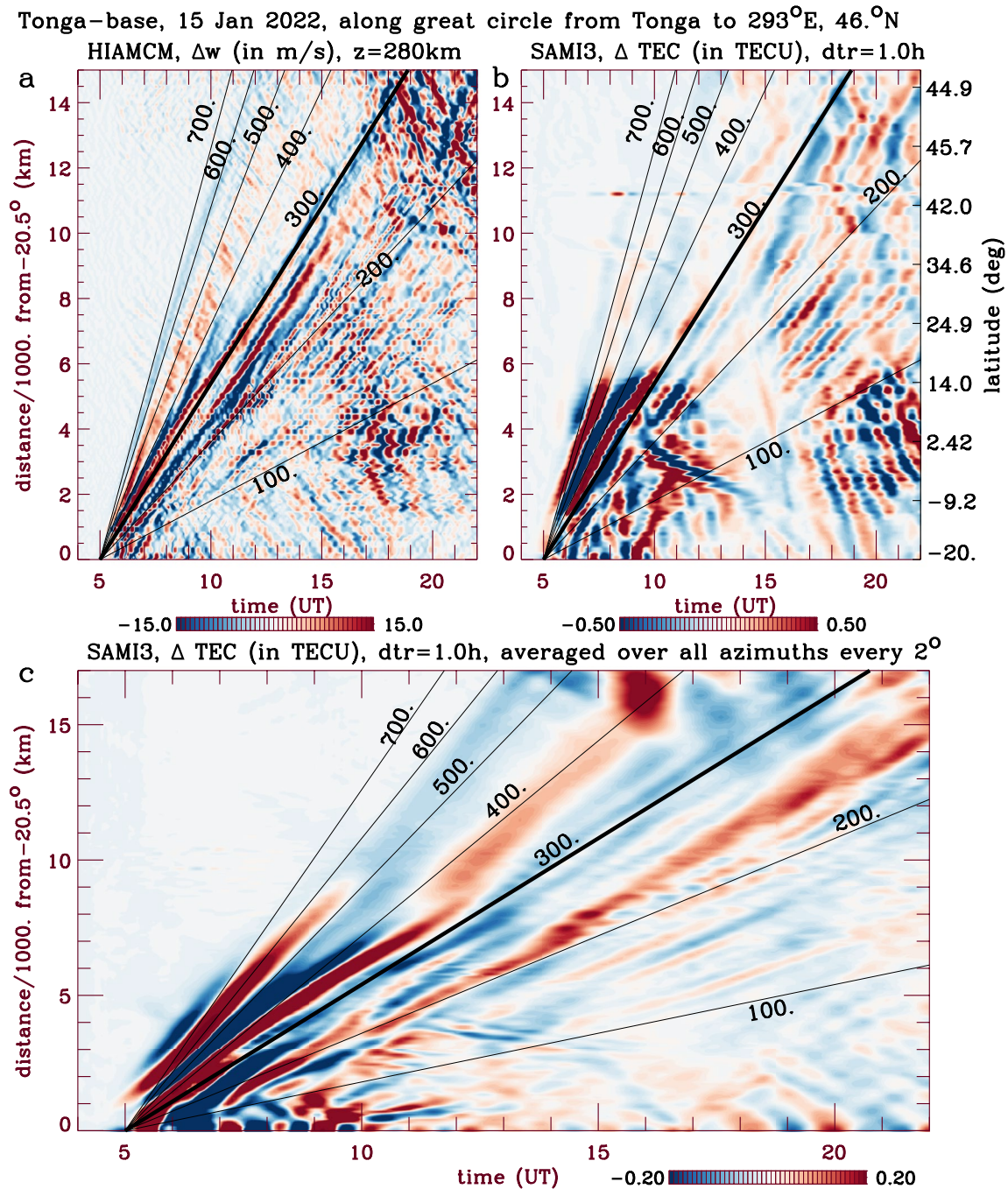


Figure 3. Model results on 15 January 2022. (a) Keogram of the HIAMCM Δw (in m/s) for the Tonga run minus the base run at $z = 280$ km as functions of time and distance from Tonga to Fredericton, Canada (293°E, 46°N). (b) Keogram of the SAMI3 ΔTEC (in TECU) for the Tonga run minus the base run along the same great circle as in (a) with a detrend window of 1 hr. (c) Keogram of the SAMI3 ΔTEC (in TECU) for the Tonga run minus the base run averaged every 2° in azimuth around Tonga from 0 to 360°. The detrend window of 1 hr is applied before averaging. Solid lines show the locations of thermospheric GWs that originated above Tonga at 5:00 UT with $c_H = 100, 200, 300, 400, 500, 600,$ and 700 m/s, as labeled, with the $c_H = 300$ m/s line being darker. The colors are oversaturated to emphasize the waves.

Figure 5 shows keograms of the dTEC response, ΔTEC , for the SAMI3 Tonga run minus the base run as functions of time and distance from Tonga along great circles to the same stations as in Figure 4 using a detrend window of 1 hr. In general (with the exception of South Africa), TIDs with similar periods and phase speeds are seen in the TEC as in w ; however, note that MSTIDs with $\tau_r < 30$ min are difficult to see in SAMI3. The absence of TIDs with $c_H \geq 500$ m/s over Australia is again due to the asymmetry of the radiated secondary GWs (seen

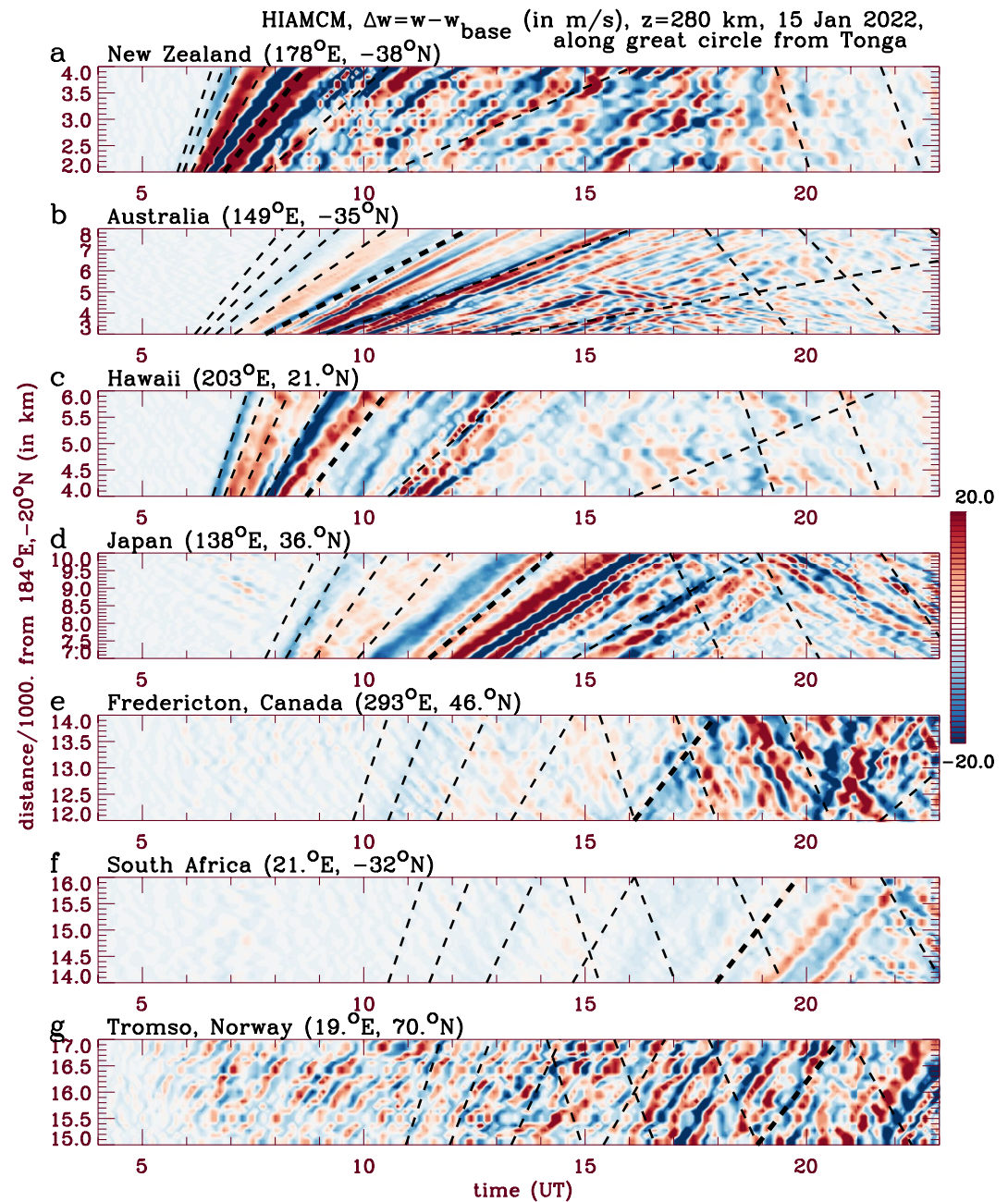


Figure 4. Keograms of the HIAMCM Δw (in m/s) on 15 January 2022 for the Tonga run minus the base run along great circles from Tonga to (a) New Zealand (178°E , 38°S); (b) Australia (149°E , 35°S); (c) Hawaii (157°W , 21°N); (d) Japan (138°E , 36°N); (e) Fredericton, Canada (67°W , 46°N); (f) South Africa (21°E , 32°S); (g) Tromsø, Norway (19°E , 70°N). Dash lines show the horizontal phase speeds of outbound and inbound thermospheric GWs that originated above Tonga at 5:00 UT in decreasing steps of 100 m/s, beginning on the left (for the outbound GWs) at 700 m/s. The $c_H = 300$ m/s dash line is darker. The colors are oversaturated to emphasize the waves.

in Figures 1 and 4) and the alignment of the GW propagation direction with **B**, as discussed above. In general, the TIDs with $c_H \approx 650\text{--}750$ m/s do not propagate further than $R > 8,000$ km from Tonga (e.g., New Zealand, Hawaii, and Japan), although extremely faint TIDs with $c_H \approx 600$ m/s may be visible over South Africa and Norway. Note that the Tonga TIDs over Fredericton have $c_H \lesssim 400$ m/s.

Figure 6 shows the data from Figure 4 of Themens et al. (2022), which displays the observed $v\text{TEC}$ using a 30 min detrend window at the same locations as in Figure 5. Although this detrend window greatly suppresses

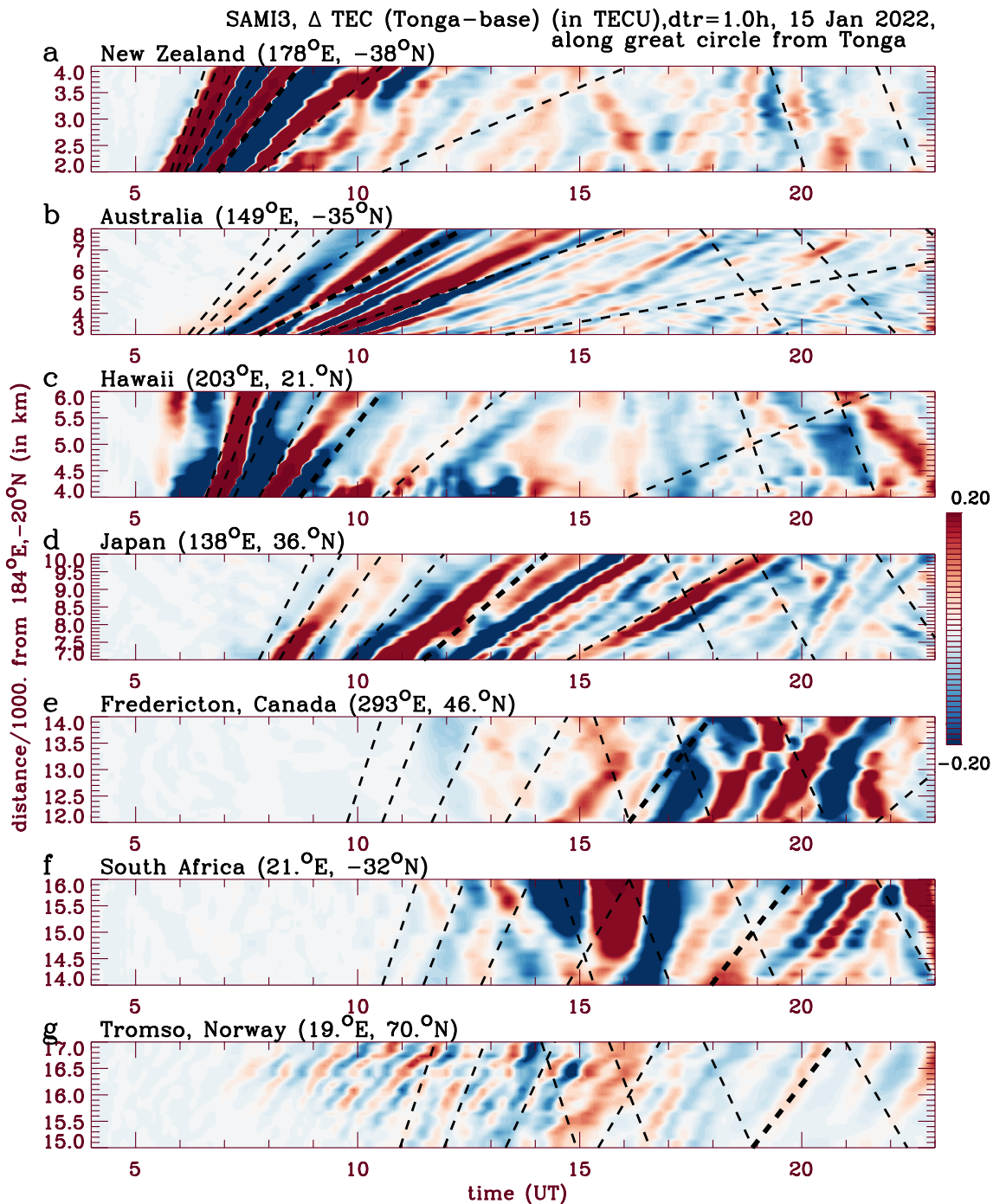


Figure 5. Keograms of the SAMI3 Δ TEC (in TECU) on 15 January 2022 for the Tonga run minus the base run along great circles from Tonga to (a) New Zealand (178°E, 38°S); (b) Australia (149°E, 35°S); (c) Hawaii (157°W, 21°N); (d) Japan (138°E, 36°N); (e) Fredericton, Canada (67°W, 46°N); (f) South Africa (21°E, 32°S); (g) Tromsø, Norway (19°E, 70°N). A detrend window of 1 hr is applied. Dash lines show the horizontal phase speeds of outbound and inbound thermospheric GWs that originated above Tonga at 5:00 UT in decreasing steps of 100 m/s, beginning on the left (for the outbound GWs) at 700 m/s. The $c_H = 300$ m/s dash line is darker. The colors are oversaturated to emphasize the waves.

the amplitudes of TIDs with $\tau_r \geq 30$ min, they are not entirely removed. Indeed, Figure 6 shows that the fastest TIDs observed over Hawaii and Japan had $\tau_r \geq 1$ hr. Figure 7 shows the same v TEC data as in Figure 6, but with a detrend window of 1 hr. The fastest waves over Hawaii, Japan, South Africa, and Norway with $\tau_r \geq 1$ hr can now be clearly seen. Comparing Figures 5 and 7, we see that the amplitudes, horizontal wavelengths and periods of the

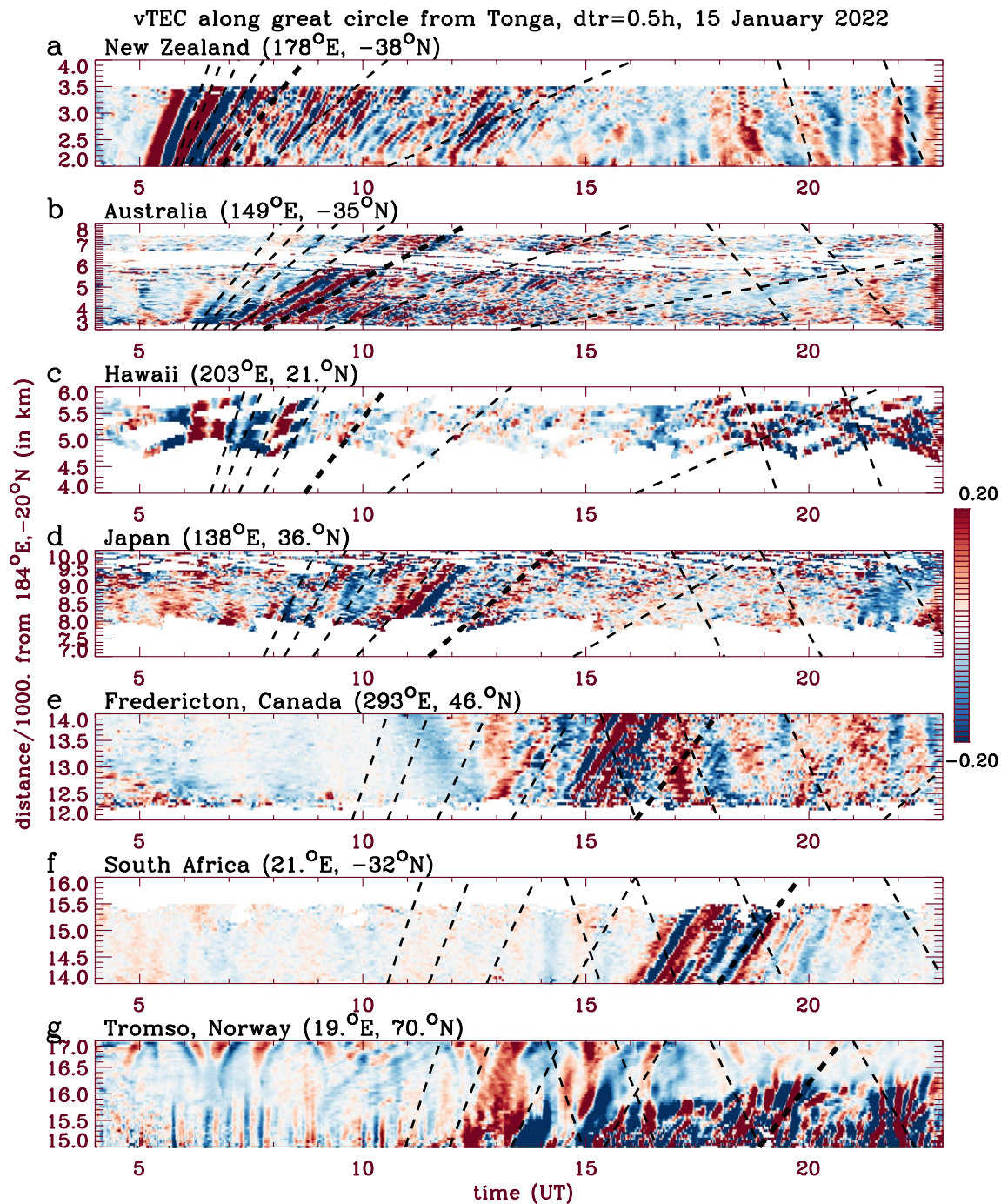


Figure 6. Vertical TEC (vTEC) anomalies on 15 January 2022 as functions of time and distance from Tonga to (a) New Zealand (178°E, 38°S); (b) Australia (149°E, 35°S); (c) Hawaii (157°W, 21°N); (d) Japan (138°E, 36°N); (e) Fredericton, Canada (67°W, 46°N); (f) South Africa (21°E, 32°S); (g) Tromsø, Norway (19°E, 70°N). A detrend window of 30 min is applied. Dash lines show the horizontal phase speeds of outbound and inbound thermospheric GWs that originated above Tonga at 5:00 UT in decreasing steps of 100 m/s, beginning on the left (for the outbound GWs) at 700 m/s. The $c_H = 300$ m/s dash line is darker. The colors are oversaturated to emphasize the waves. This vTEC data is from (Themens et al., 2022, their Figure 4).

modeled TIDs agree well with the observed TIDs at these stations. Differences over Norway and Canada could be due to the geomagnetic activity which occurred during the Tonga event (Shinbori et al., 2022).

It is interesting to note that the TID amplitudes are faint from 10:00–16:00 UT over Hawaii in both the SAMI3 dTEC and vTEC in Figures 5 and 7, respectively, even though secondary GWs are propagating over Hawaii at

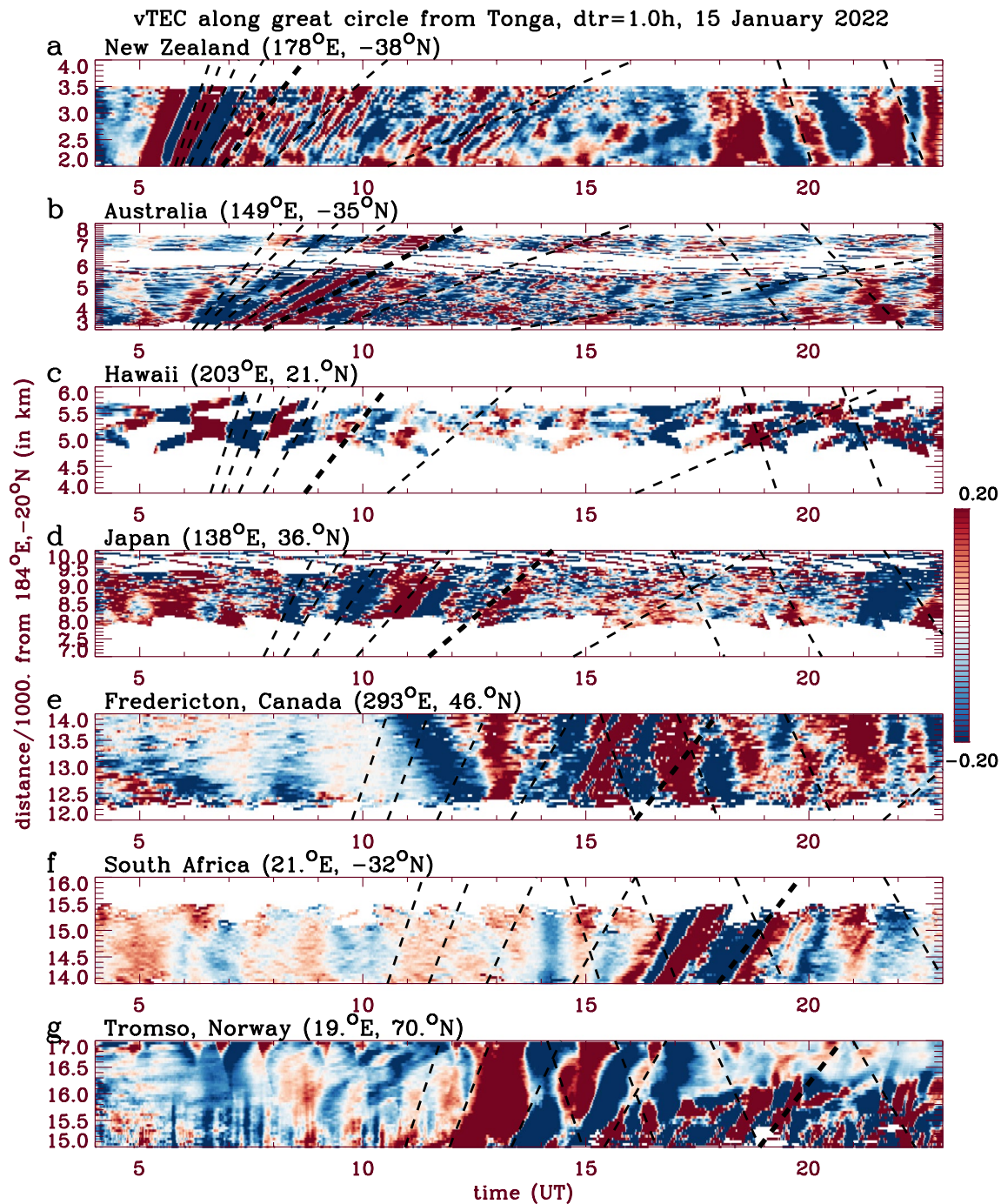


Figure 7. Same as Figure 6, but for a detrend window of 1 hr.

that time (see Figure 4). This time period coincides with the occurrence of plasma bubbles (see rows 3–4 of Figure 2). Figures 8a and 8b shows the detrended TEC, dTEC, for the SAMI3 base and Tonga runs, respectively, at 9:30 UT, using a 1 hr detrend window. Although plasma bubbles appear over the Pacific Ocean in the base run, they are southwest of Hawaii. In the Tonga run, however, new plasma bubbles triggered by the secondary GWs from Tonga occur over Hawaii (Huba et al., 2023). Figures 8c and 8d shows the corresponding dTEC at 11:30 UT. The EPBs over and south of Hawaii are triggered by the secondary GWs from Tonga. Thus the significantly suppressed TID amplitudes at 10–16 UT could be due to the presence of plasma bubbles, ionospheric effects at sunset, and/or lower electron densities on the nightside. In either case, the observed suppression of TIDs confirms the model results.

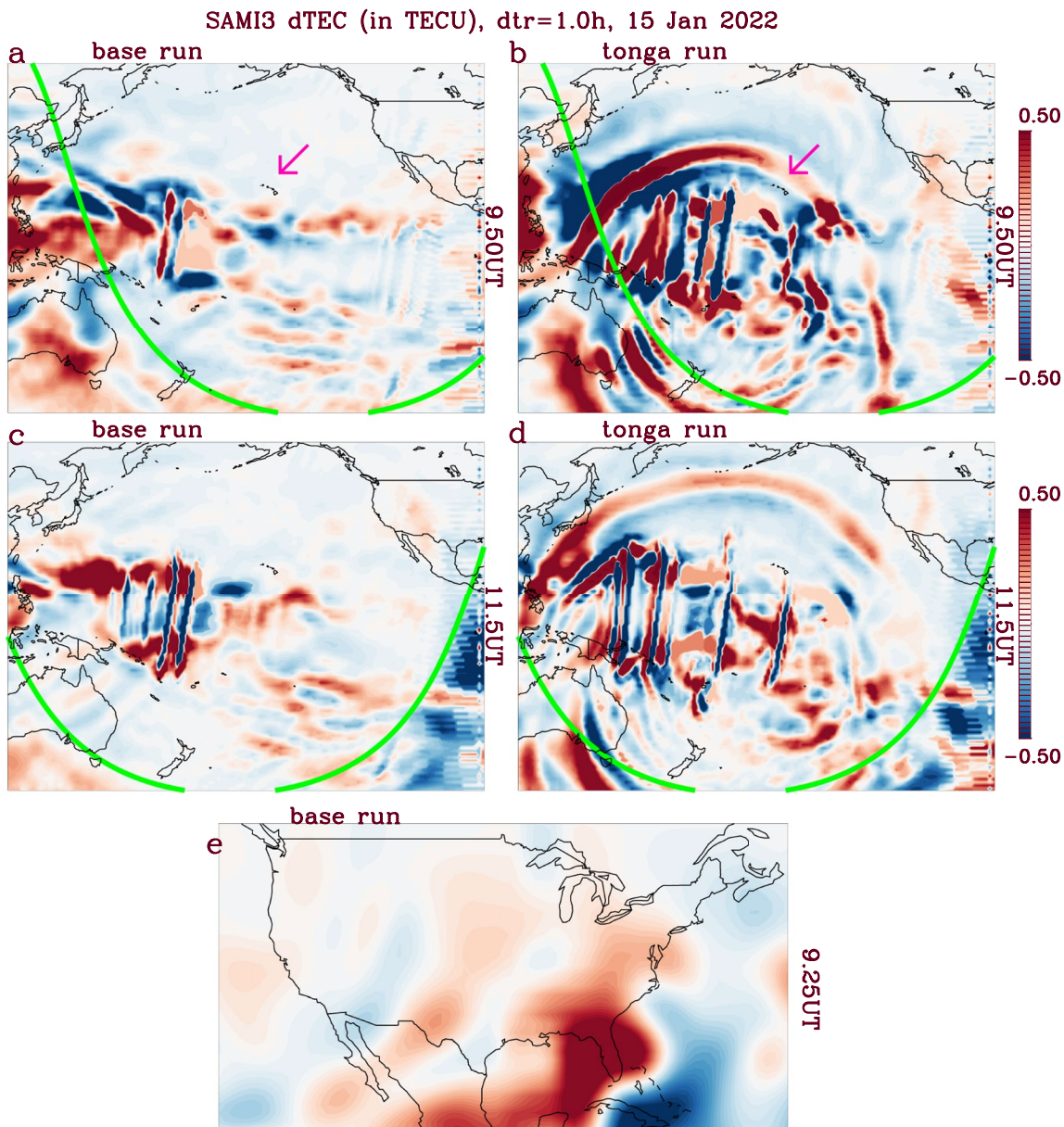


Figure 8. dTEC from the SAMI3 on 15 January 2022 using a 1 hr detrend window. Base run (a) and Tonga run (b) at 9:30 UT over the Pacific Ocean. (c)–(d) Same as (a)–(b) but at 11:30 UT. The green solid lines show the solar terminator. The pink arrows point to Hawaii in (a)–(b). (e) Base run at 9:15 UT over the CONUS. The colors are oversaturated to see the waves.

We now investigate if EPBs were present over Hawaii during this time. We utilize ground-based GPS observations from the GPS receiver at Naalehu, Hawaii (KUAH), for elevation angles $>30^\circ$. These observations are from a Septentrio PolarX5 receiver at 1-Hz resolution, thereby enabling the monitoring of scintillation using the Carrier to Noise Ratio (CNR) (Mrak et al., 2020). Figure 9a shows the daily v TEC from the KUAH receiver, derived by minimizing the standard deviation over all lines of sight (Mrak et al., 2021). Here, different colors are used to distinguish observations from different receiver-satellite pairs. Two large-amplitude “leading” LSTIDs arrive at the receiver’s field of view just before 6 UT, as indicated by the black arrows. The second LSTID is no longer visible at ~ 9 UT. These times agree well with the two LSTIDs seen in Figures 6c and 7c. Figure 9b shows the daily CNR; no measurable scintillation is seen at the GPS frequencies. Figure 9c shows the single-receiver detrended TEC (dTEC) using a 1-hr detrending window. The LSTIDs at ~ 5 – 9 UT have large peak-to-peak amplitudes of ~ 2 – 2.5 TECU. The first and second LSTIDs have periods of $\tau_1 \sim 90$ and ~ 60 min, respectively. Because the background TEC is extremely low after 10 UT ($\lesssim 1$ TECU), it is difficult to see perturbations at that time. Figure 9d

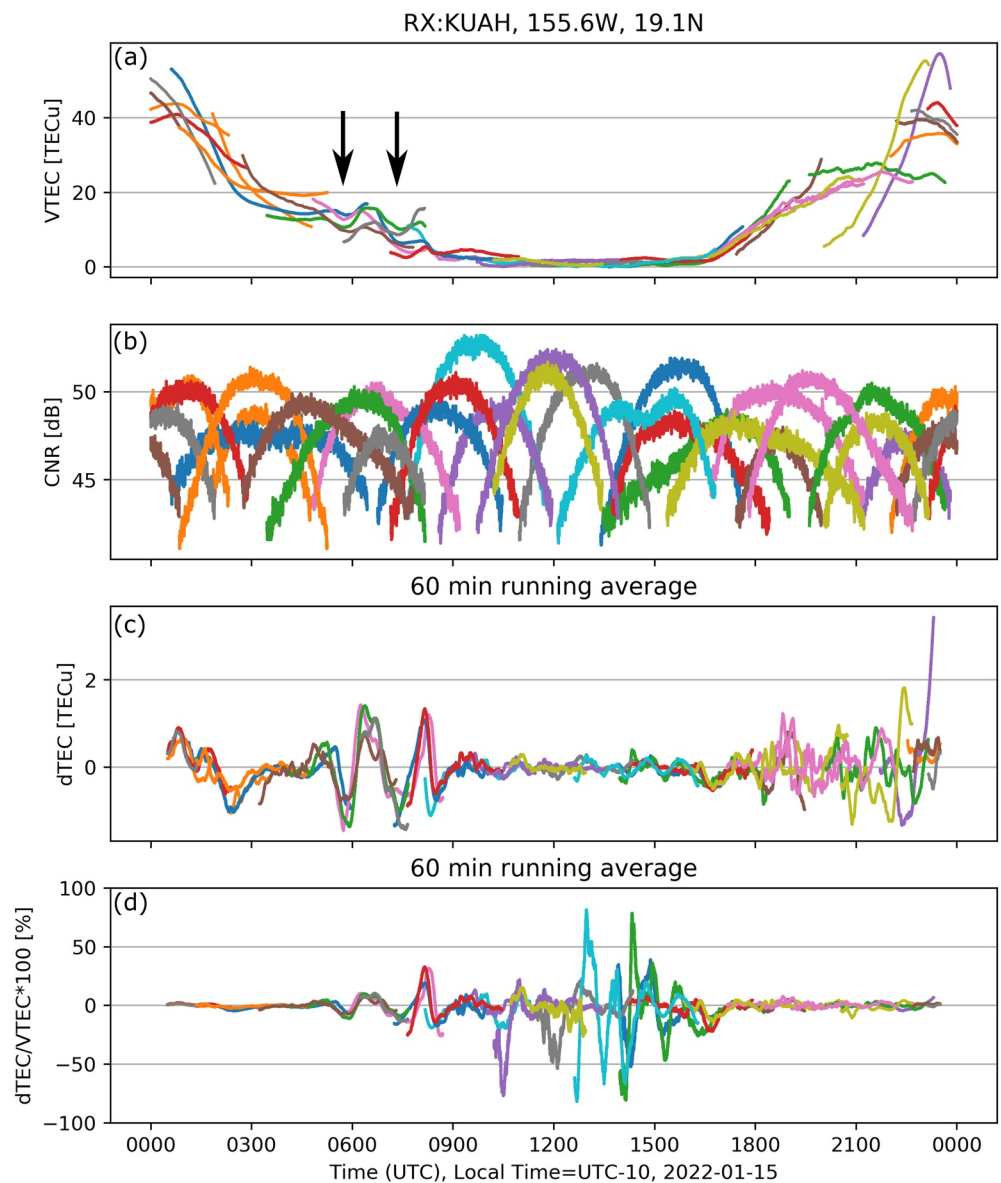


Figure 9. Ground-based ionospheric GPS observations from Hawaii's KUAH receiver with 1-Hz resolution on 15 January 2022. (a) Vertical Total Electron Content (VTEC) (in TECU). Black arrows show the arrival of two large-amplitude LSTIDs. (b) Carrier to Noise Ratio (CNR) (in dB). (c) Differential TEC (dTEC) (in TECU) detrended with a 1-hr running average window. (d) dTEC divided by the mean VTEC (in %). Different colors show the results from different satellites.

shows the relative TEC perturbation (in %), $100 \text{ dTEC}/\text{mean}(\text{vTEC})$, where $\text{mean}(\text{vTEC})$ is the mean background TEC obtained with the 1-hr sliding window. Ionospheric perturbations are clearly present at 11:00–17:00 UT. The perturbations show both periodic signatures of the passing GWs (see Figure 4c) and small-scale perturbations at ~ 12 UT (gray and yellow lines). The latter is due to plasma irregularities, which could be due to EPBs. These irregularities are in agreement with the SAMI3 results shown in Figures 2h and 8d, which shows that the northern edge of the plasma irregularities (EPBs) were over Hawaii. These irregularities did not cause fluctuations in the CNR because of the very low background TEC. These observations indicate that either the trailing GW packets after 10 UT (with smaller periods) facilitated the EPBs, or that the EPBs were generated by the leading GW packets west of Hawaii that drifted eastward with time and reached Hawaii at ~ 12 UT. Both explanations are likely, because it was demonstrated that slower GWs with $\tau_r < 30$ min are the more potent source of EPBs (Krall et al., 2013), and because EPBs normally exhibit eastward drift. Thus, Figure 9d demonstrates that plasma irregularities were likely present over Hawaii, as simulated by SAMI3, although with a slight time delay.

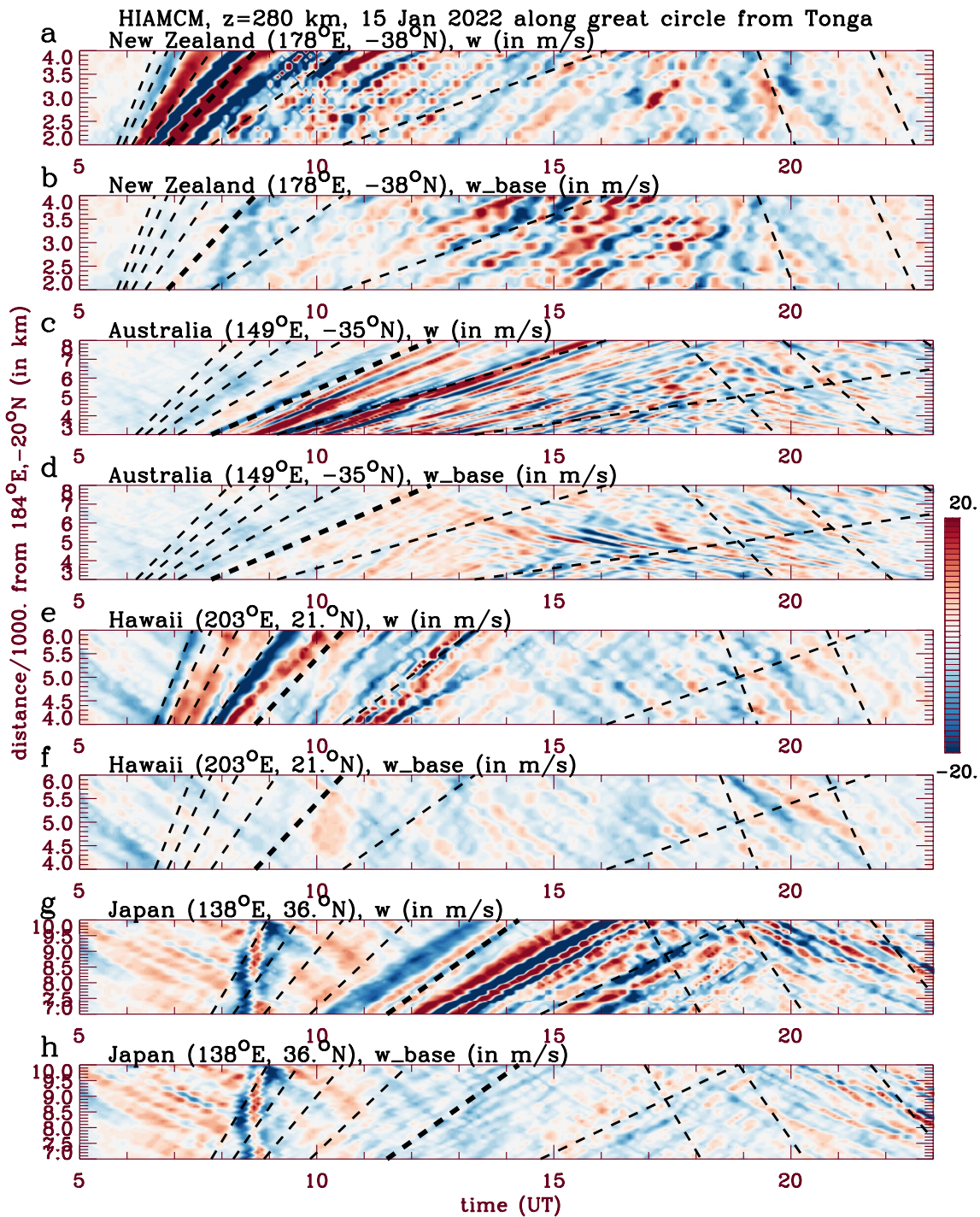


Figure 10. Keogram of the HIAMCM w for the Tonga run (a) and w_{base} for the base run (b) along a great circle from Tonga to New Zealand (178°E , 38°S) on 15 January 2022. (c)–(d) Same as (a)–(b) but along a great circle from Tonga to Australia (149°E , 35°S). (e)–(f) Same as (a)–(b) but along a great circle from Tonga to Hawaii (157°W , 21°N); (g)–(h) Same as (a)–(b) but along a great circle from Tonga to Japan (138°E , 36°N). Dash lines show the horizontal phase speeds of outbound and inbound thermospheric GWs that originated above Tonga at 5:00 UT in decreasing steps of 100 m/s, beginning on the left (for the outbound GWs) at 700 m/s. The $c_H = 300$ m/s dash line is darker. The colors are oversaturated to emphasize the waves.

3.3. Modeled GWs at Stations Worldwide From Tonga and Base Runs

We now investigate if the GWs observed toward the end of 15 January over New Zealand, Australia, Hawaii and Japan in Figure 4 are “inbound” GWs from Tonga. Figures 10a and 10b shows keograms of the vertical wind from

the HIAMCM Tonga run (w) and the base run (w_{base}), respectively, at $z = 280$ km on 15 January as functions of time and distance along the great circles from Tonga to New Zealand. The waves that could be “inbound” GWs in the Tonga run occur after 19:00 UT in Figure 10a. These waves have similar slopes as the GWs from Tonga (dash lines). However, these waves also appear in w_{base} in Figure 10b; therefore these GWs are not inbound GWs from Tonga. Figures 10a and 10b shows that it can be quite tricky to correctly-diagnose Tonga TIDs from the $v\text{TEC}$. Figures 10c–10h shows the corresponding keograms over Australia, Hawaii and Japan. It is unlikely that the GWs after 18:00 UT in w over Australia and Hawaii are inbound Tonga GWs because similar GWs appear in w_{base} . However, the GWs in w after 20:00 UT over Japan with $c_H \geq 500\text{--}600$ m/s may be inbound Tonga GWs because their amplitudes are significantly larger than the corresponding GW amplitudes in w_{base} . The fact that the angles are somewhat different than the dash lines can occur because of refraction from a non-zero background wind, since the dash lines do not take into account changing background winds.

3.4. Secondary GWs and TIDs Over the CONUS and South America

Figure 11 (left column) shows the temperature response, $\Delta T = T - T_{\text{base}}$, over the CONUS, computed from the HIAMCM Tonga run minus the base run at $z = 280$ km at 11:00, 14:00, 18:00, and 22:00 UT on 15 January 2022. Figure 11 (right column) shows the $d\text{TEC}$ response, ΔTEC , computed from the SAMI3 Tonga run minus the base run at the same times using a 1 hr detrend window. The TIDs generally “follow” the GWs (especially for $\lambda_H \leq 2,000$ km), although they are conspicuously absent at high latitudes in the northern CONUS and Canada. This may occur because \mathbf{B} is nearly vertical there and the GW propagation direction is close to horizontal, and/or because photoionization is reduced at high latitudes. Note that large-scale GWs and LSTIDs reach the eastern CONUS by 11:00 UT with $c_H \approx 600$ m/s.

Figure 12 (left column) shows the temperature response, $\Delta T = T - T_{\text{base}}$, over South America, computed from the HIAMCM Tonga run minus the base run at $z = 280$ km at 10:00, 12:00, 14:00, and 16:00 UT on 15 January 2022. Figure 12 (right column) shows ΔTEC computed from the SAMI3 Tonga run minus the base run at the same times. The TIDs generally follow the GWs over South America. Large-scale GWs and LSTIDs reach the southern tip of South America at $\sim 9:30$ UT with $c_H \approx 600$ m/s, $\lambda_H \approx 3,000\text{--}4,000$ km and $\tau_r \approx 1.3\text{--}1.9$ hr.

Figures 13a and 13b shows keograms of the $d\text{TEC}$ response, ΔTEC , for the SAMI3 Tonga run minus the base run as functions of time and latitude/longitude over the western CONUS at 35.5°N and 240°E , respectively. The progression of LSTIDs with large periods at $\sim 8:00\text{--}10:00$ UT ($\tau_r \approx 1\text{--}3$ hr) to smaller periods at later times ($\tau_r \approx 40\text{--}90$ min) is seen. Figures 13c and 13d shows the corresponding keograms of ΔTEC over South America at 29.5°S and 290°E , respectively. The progression of LSTIDs with large periods at early times ($\tau_r \approx 3$ hr) to smaller periods at later times ($\tau_r \approx 60$ min) is seen.

4. TIDs Observed in the $v\text{TEC}$ Over the CONUS and South America

The $v\text{TEC}$ is calculated from GPS and GLONASS constellations every 30 s which ignores the phase ambiguity and satellite and receiver biases (e.g., Figueiredo et al., 2017; Tsugawa et al., 2007). The $v\text{TEC}$ is detrended by subtracting a 1, 2, or 3-hr running mean (centered at ± 30 , ± 60 , and ± 90 min, respectively) from the $v\text{TEC}$ time series. Figures 14a and 14b shows horizontal slices of the $v\text{TEC}$ over the nighttime CONUS at 8:36 and 9:14 UT using a 3 hr detrend window. The fastest TIDs from Tonga are seen propagating over California, Oregon and Washington, as indicated by the purple arrows. The parameters of these TIDs, as extracted manually from the $v\text{TEC}$ maps and keograms (see below), are $c_H = 682 \pm 100$ m/s and $\tau_r = 87 \pm 2$ min, and azimuth $\psi \approx 70^\circ$. These are LSTIDs, with $\lambda_H = c_H \tau_r = 3560 \pm 604$ km. Comparing with the model results shown in Section 3, we see that the arrival time and parameters of these LSTIDs agree well with that of the modeled LSTIDs. Movie S1 shows the $v\text{TEC}$ (in TECU) over the CONUS using a 3 hr detrend window. There are also LSTIDs that propagate south and southeastward over the central CONUS in Figures 14a and 14b; some of these waves may be from a geomagnetic storm at $\sim 22:00$ UT on 14 January, which had $Kp \sim 2\text{--}3.3$ during this time (e.g., Heki, 2022; Shinbori et al., 2022). However, Figure 8e shows the $d\text{TEC}$ for the SAMI3 base run, which does not contain geomagnetic forcing effects. Southeastward-propagating LSTIDs are seen over the central CONUS. Therefore, some of the TIDs over the central CONUS in Figures 14a and 14b may be induced by higher-order GWs from wintertime sources over North America, such as mountain waves and the polar vortex (Becker & Vadas, 2020; Becker, Vadas, et al., 2022; Heale et al., 2020; Vadas & Becker, 2019; Vadas, Becker, Bossert, et al., 2023).

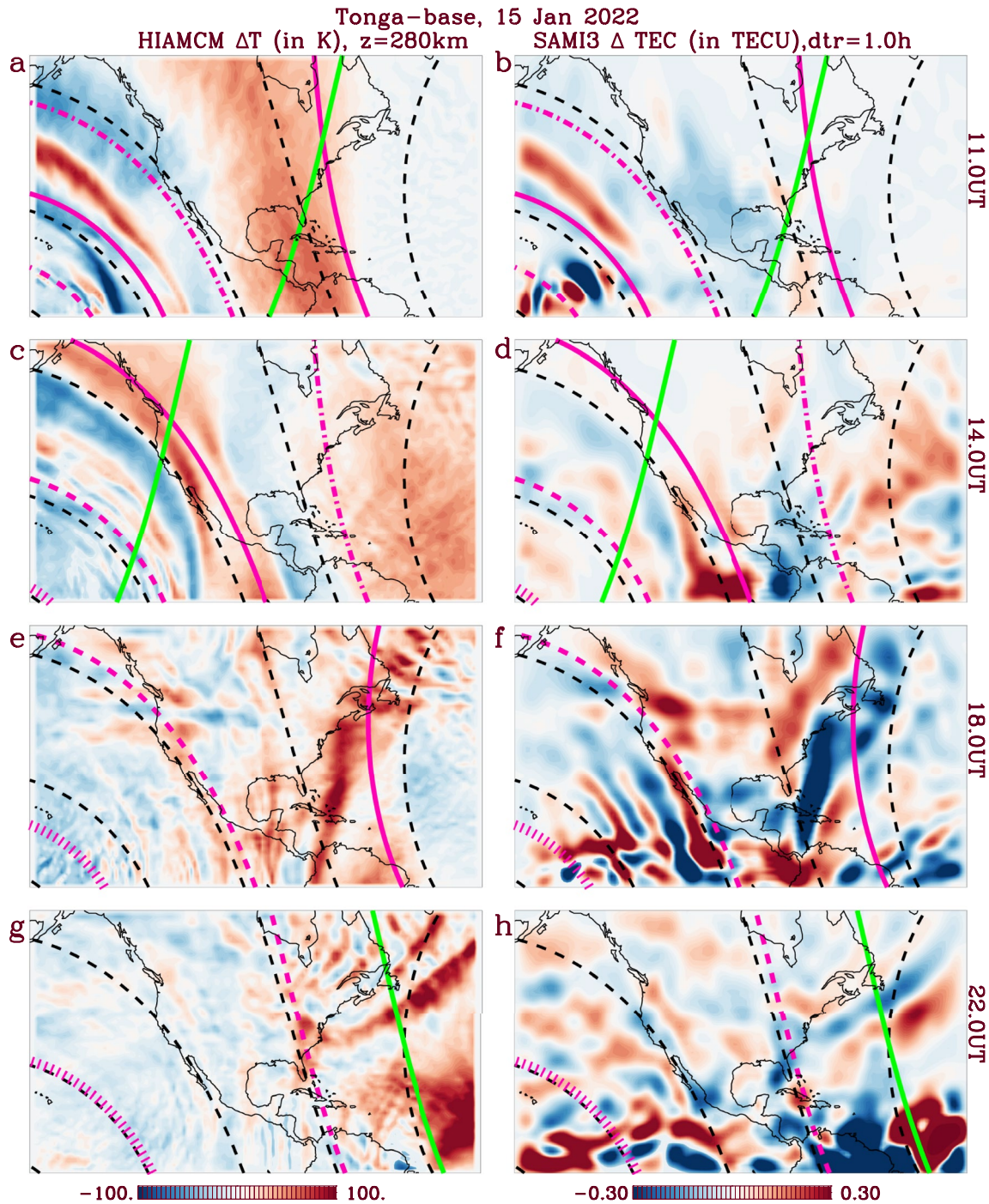


Figure 11. (a) ΔT (in K) from the HIAMCM Tonga run minus the base run on 15 January 2022 at $z = 280$ km at 11:00 UT over the CONUS. (b) Same as in (a), but for ΔTEC (in TECU) for the SAMI3 Tonga run minus the base run with a 1 hr detrend window. Rows (2–4) Same as row 1, but for 14:00, 18:00 and 22:00 UT, respectively. Pink dot, dash, solid, dash-dot, and dash-dot-dot-dot lines show the locations of thermospheric GWs that originated above Tonga at 5:00 UT with $c_H = 100, 200, 300, 400,$ and 600 m/s, respectively. Black dash lines show equi-distances from Tonga in 3,000 km intervals. Green solid lines show the solar terminator. The colors are oversaturated to see the waves.

Figures 14c and 14d show the same $v\text{TEC}$ slices as in Figures 14a and 14b, but detrended with a 1 hr running mean. As expected, the fastest LSTIDs from Tonga are not visible over the western CONUS because this restricted analysis method removes the LSTIDs with $\tau_r > 1$ hr. This is why Zhang et al. (2022) did not observe these fastest LSTIDs from Tonga over the CONUS.

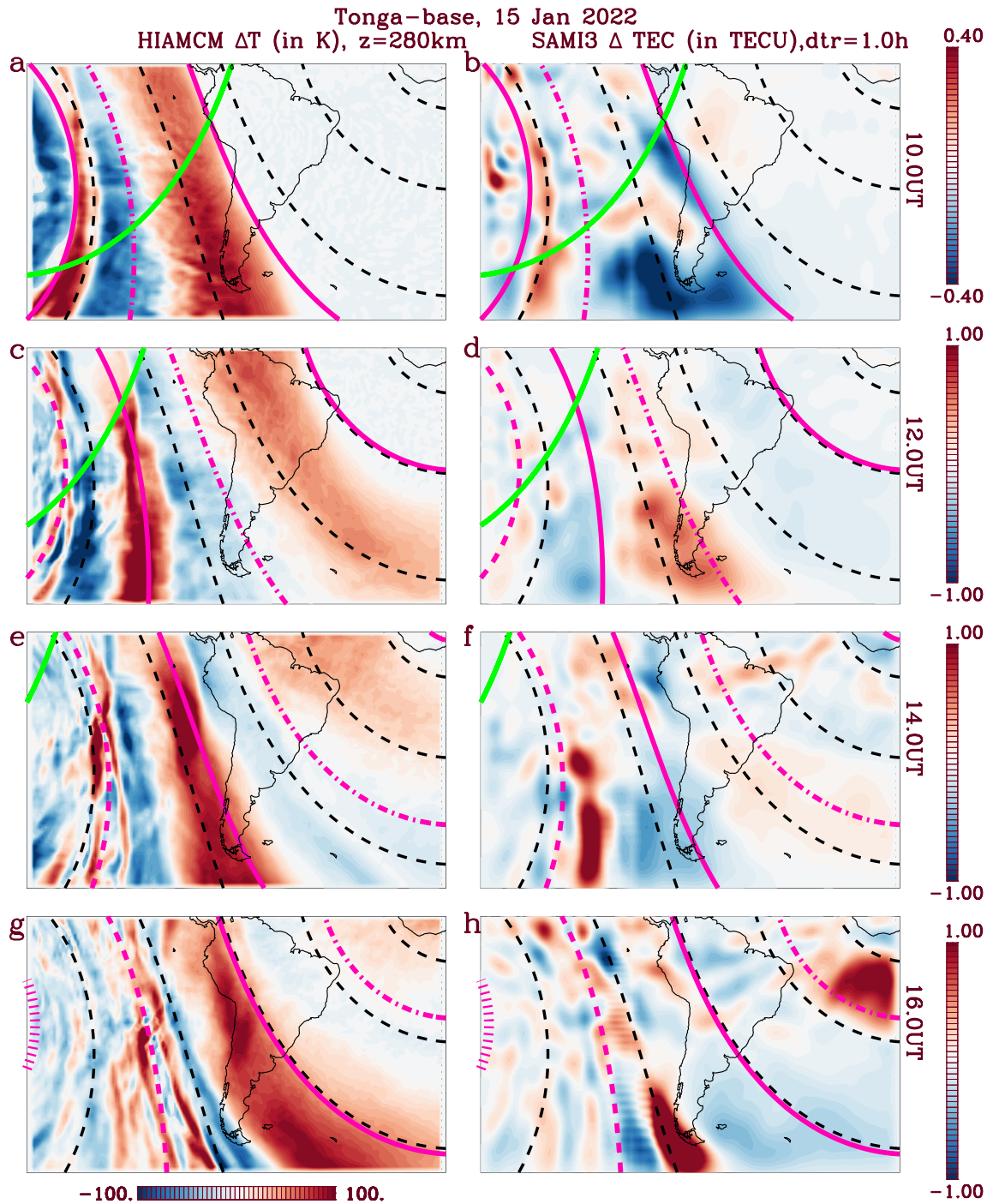


Figure 12. (a) ΔT (in K) from the HIAMCM Tonga run minus the base run on 15 January 2022 at $z = 280$ km at 10:00 UT over South America. (b) Same as in (a), but for ΔTEC (in TECU) for the SAMI3 Tonga run minus the base run with a 1 hr detrend window. Rows (2–4) Same as row 1, but for 12:00, 14:00, and 16:00 UT, respectively. Pink dot, dash, solid, dash-dot, and dash-dot-dot-dot lines show the locations of thermospheric GWs that originated above Tonga at 5:00 UT with $c_H = 100, 200, 300, 400,$ and 600 m/s, respectively. Black dash lines show equi-distances from Tonga in 3,000 km intervals. Green solid lines show the solar terminator. The colors are oversaturated to see the waves.

Figures 15a and 15b show horizontal slices of the $v\text{TEC}$ over South America at 9:16 and 10:00 UT (during the daytime). Here, we detrend the $v\text{TEC}$ with a 2 hr running mean to enable observation of TIDs with $\tau_r \leq 2$ hr (We use a somewhat smaller running mean here than in Figures 14a and 14b because there are less GNSS receivers here than over the US.) The fastest TIDs from Tonga are seen over southern South America at these

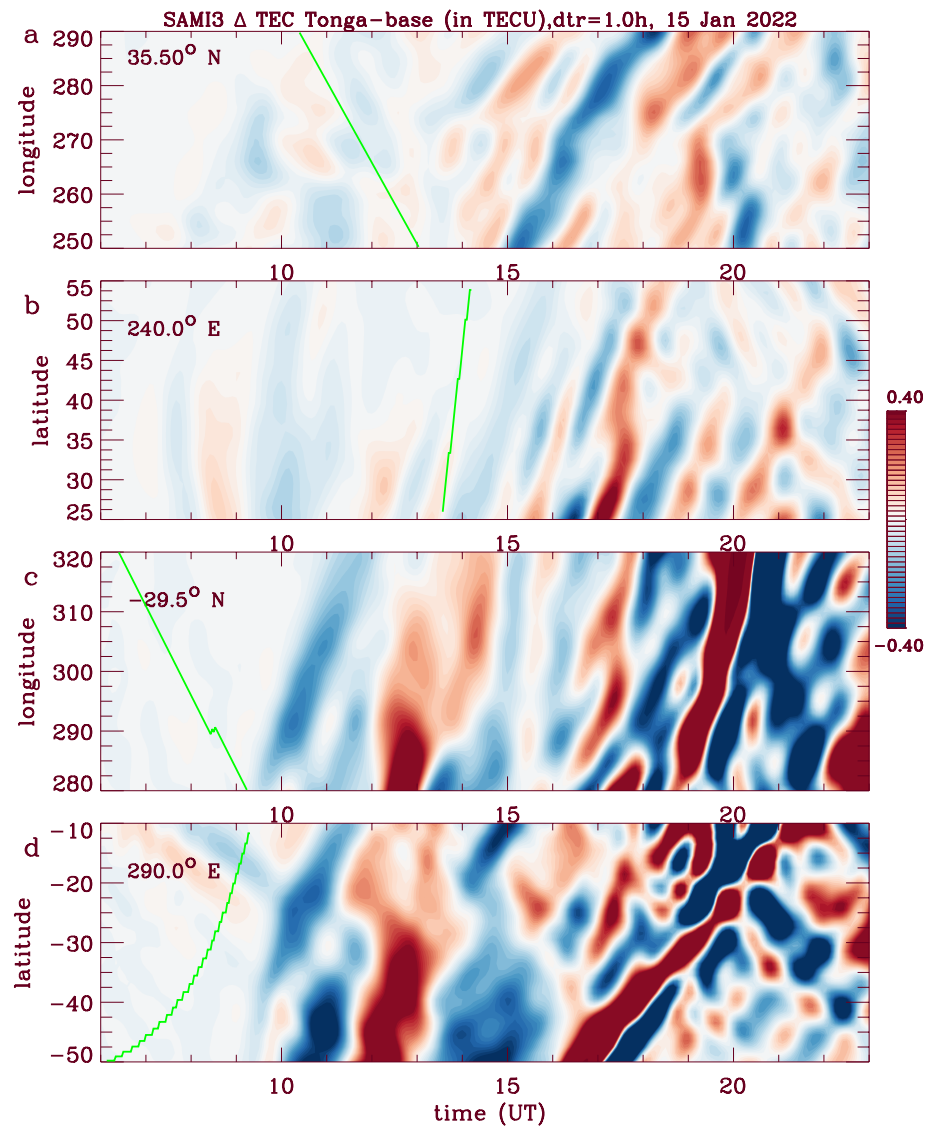


Figure 13. Keograms of Δ TEC (in TECU) computed from the SAMI3 Tonga run minus the base run on 15 January 2022 as functions of time and latitude/longitude using a 1 hr detrend window. The TIDs over the western CONUS are shown at (a) 35.5°N , (b) 240°E . The TIDs over South America are shown at (c) 29.5°S and (d) 290°E . Green solid lines show the sunrise and sunset terminators.

times, as indicated by the purple arrows. The parameters of the fastest TIDs, as extracted manually from the $v\text{TEC}$ maps and keograms (see below), are $c_H = 675 \pm 58$ m/s, $\tau_r = 78 \pm 6$ min and $\psi \simeq 40^\circ$. These are LSTIDs, with $\lambda_H = 3,159 \pm 514$ km. Comparing with the model results shown in Section 3, we see that the arrival time and parameters of these LSTIDs agree well with the modeled TIDs. Movie S2 shows the $v\text{TEC}$ (in TECU) over South America using a 2 hr detrend window. Figure 15c shows a horizontal slice of the $v\text{TEC}$ at 13:00 UT using a 1 hr detrend window. Northeastward-propagating MSTIDs from Tonga are observed with $\lambda_H \simeq 479 \pm 88$ km, $c_H = 399 \pm 124$ m/s, $\tau_r = 20 \pm 5$ min, and $\psi \simeq 32 \pm 5^\circ$. Figure 15d shows a horizontal slice of the $v\text{TEC}$ at 18:00 UT using a 1 hr detrend window. The MSTIDs from Tonga have $\lambda_H \simeq 505 \pm 70$ km, $c_H = 350 \pm 88$ m/s, $\tau_r = 24 \pm 5$ min, and $\psi \simeq 24 \pm 4^\circ$ at this time.

Figures 16a and 16b show keograms of the $v\text{TEC}$ over the western coast of the CONUS detrended with a 3 hr running mean. The fastest TIDs from Tonga are LSTIDs, and arrive there at $\sim 8:30$ UT with $c_H \simeq 675$ m/s and $\tau_r \simeq 90$ min (see above), as indicated by the purple arrow. These TIDs are not observed further east and north of $30\text{--}40^\circ\text{N}$ and $235\text{--}245^\circ\text{E}$ ($115\text{--}125^\circ\text{W}$), in good agreement with the model results from Section 3. Figures 16c

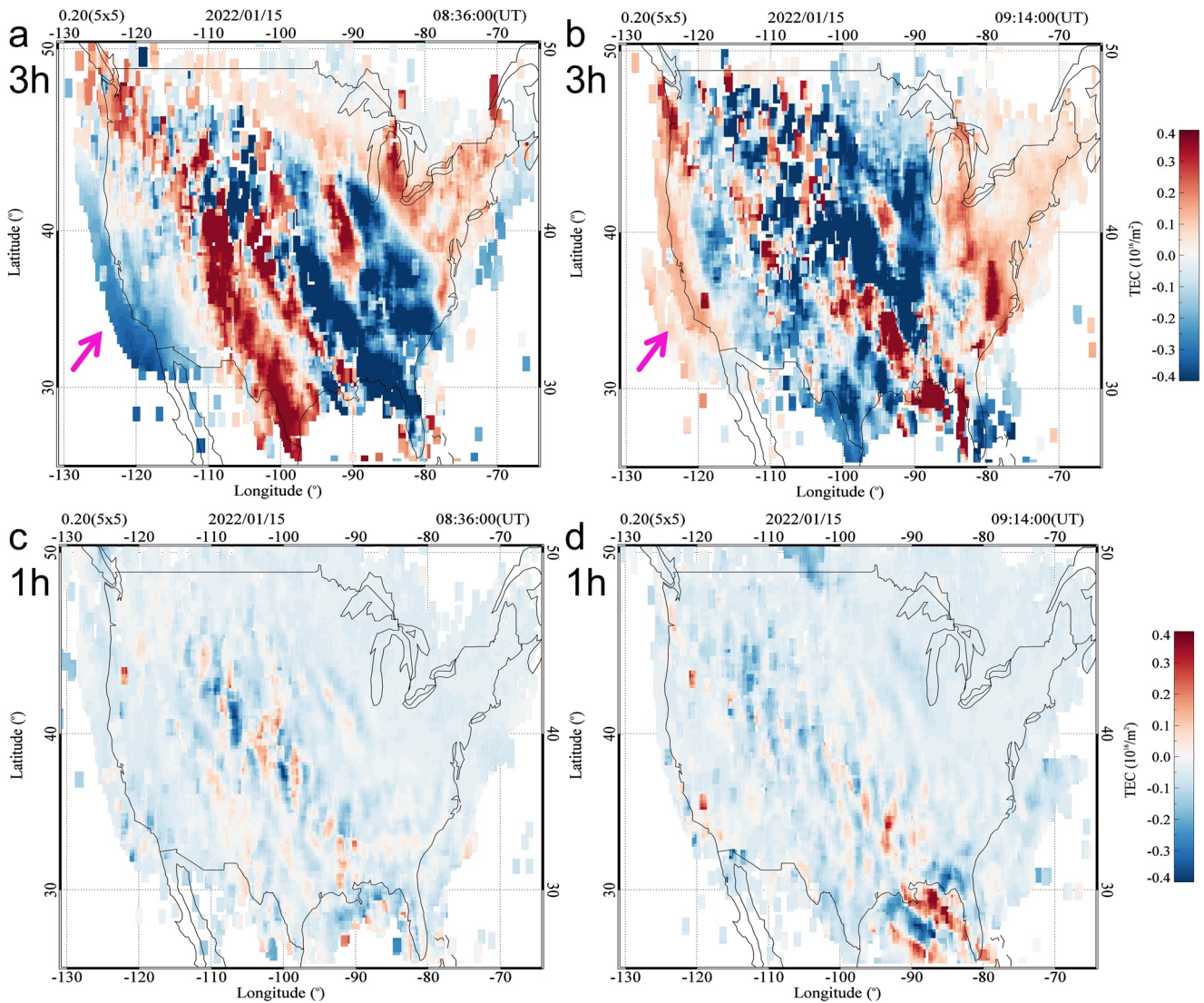


Figure 14. vTEC over the CONUS on 15 January 2022 at 8:36 UT (a) and 9:14 UT (b) using a 3 hr detrend window. (c)–d) Same as in (a)–(b), except using a 1 hr detrend window. Purple arrows indicate the fastest LSTIDs from Tonga in (a)–(b).

and 16d show keograms of the vTEC over South America detrended with a 2 hr running mean. The fastest TIDs from Tonga are LSTIDs, and reach South America at 9:00–9:30 UT at 290°–310°E (50°–70°W), and 20°–45°S, as indicated by the purple arrow. These LSTIDs have an extended coherent structure, with $c_H \approx 675$ m/s and $\tau_r = 80$ min (see above).

Figures 17a and 17b show keograms of the vTEC over the CONUS at 35°N and 90°W, and Figures 17c and 17d show keograms of the vTEC over South America at 30°S and 70°W. These keograms are detrended with a 1 hr running mean. These keograms look quite different from Figure 16 due to the lack of LSTIDs with $\tau_r > 1$ hr. The MSTIDs arrive over the CONUS and South America at ~11–12 UT with $\tau_r \approx 20$ –40 min. These TIDs are confined east of 100°W and south of 45°N over the CONUS. Note that MSTIDs are not observed at either location at ~15:00–17:00 UT, presumably due to wind filtering by the background wind.

5. Observation of LSTIDs by Ionosondes in Colorado and Idaho, USA

Figure 18 shows the parameters of the manually processed ionosonde measurements on 15 January 2022 over Boulder, CO, USA (first column) and Idaho Falls, ID, USA (second column) from the Lowell DIDBase using the SAO-X Explorer software from the Global Ionospheric Radio Observatory (GIRO) (Reinisch & Galkin, 2011). Row

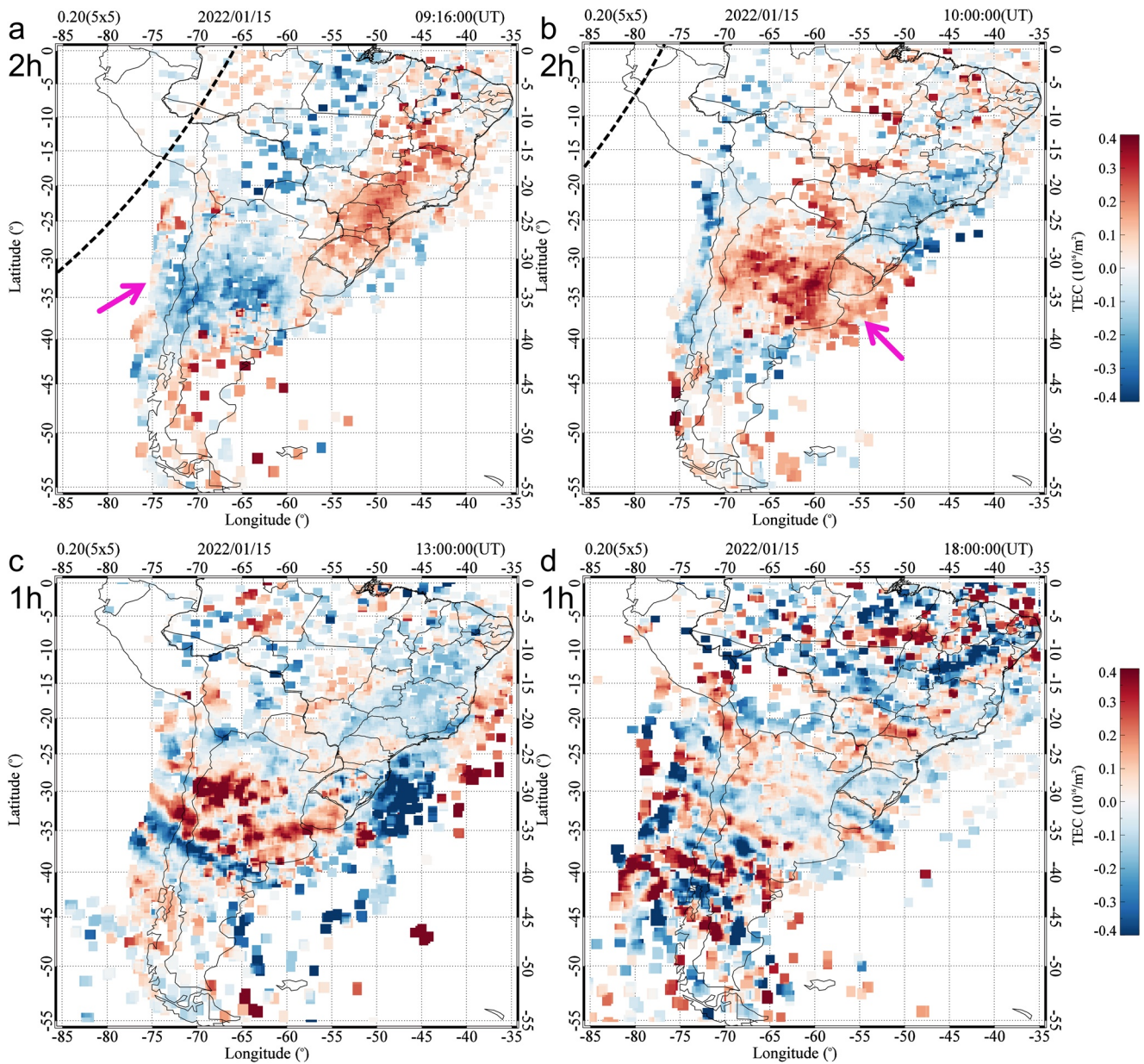


Figure 15. vTEC over South America on 15 January 2022 at (a) 9:16 UT, (b) 10:00 UT, (c) 13:00 UT, and (d) 18:00 UT. We detrend with a 2 hr running mean in (a)–(b), and with a 1 hr running mean in (c)–(d). Purple arrows indicate the fastest LSTIDs from Tonga in (a)–(b).

1 shows the critical frequency of the F2 layer, foF2 (diamonds) and the quiet-time prediction, foF2p (dotted line). Large-amplitude LSTIDs, which clearly stands out from the quiet-time prediction, are seen at 7–13 UT, with peaks at ≈ 8.8 and 11.6 UT at both locations. These LSTIDs have an apparent period of ≈ 2.8 hr. Row 2 shows the height of the peak of the F2 layer, hmF2 (diamonds). The hmF2 decreases by ≈ 110 and 130 km at Boulder and Idaho Falls, respectively, to minimum values at ~ 9 UT, then increases again by ≈ 125 –150 km to maximum values at ~ 11 UT, then decreases again by ≈ 130 –140 km to minimum values at ~ 12 UT. The period of this oscillation is ≈ 2.8 hr. The pink arrows highlight the wave structures associated with these drops. Row 3 shows the MUF(3000)F2, which is the Maximum Useable Frequency at a ground distance of 3,000 km. MUF(3000)F2 is an URSI-standard ionogram-derived characteristic which has often been used to study TIDs (Aryal et al., 2019; Altadill, et al., 2020; Verhulst et al., 2022). (Note that MUF(3000)F2 is more sensitive to the passage of TIDs than foF2 because it also contains information about the change in the layer height and thickness associated with the TIDs.) Again, a large-amplitude LSTID with a ≈ 2.8 hr period is seen at both locations, with peaks at the same times as the peaks in the foF2.

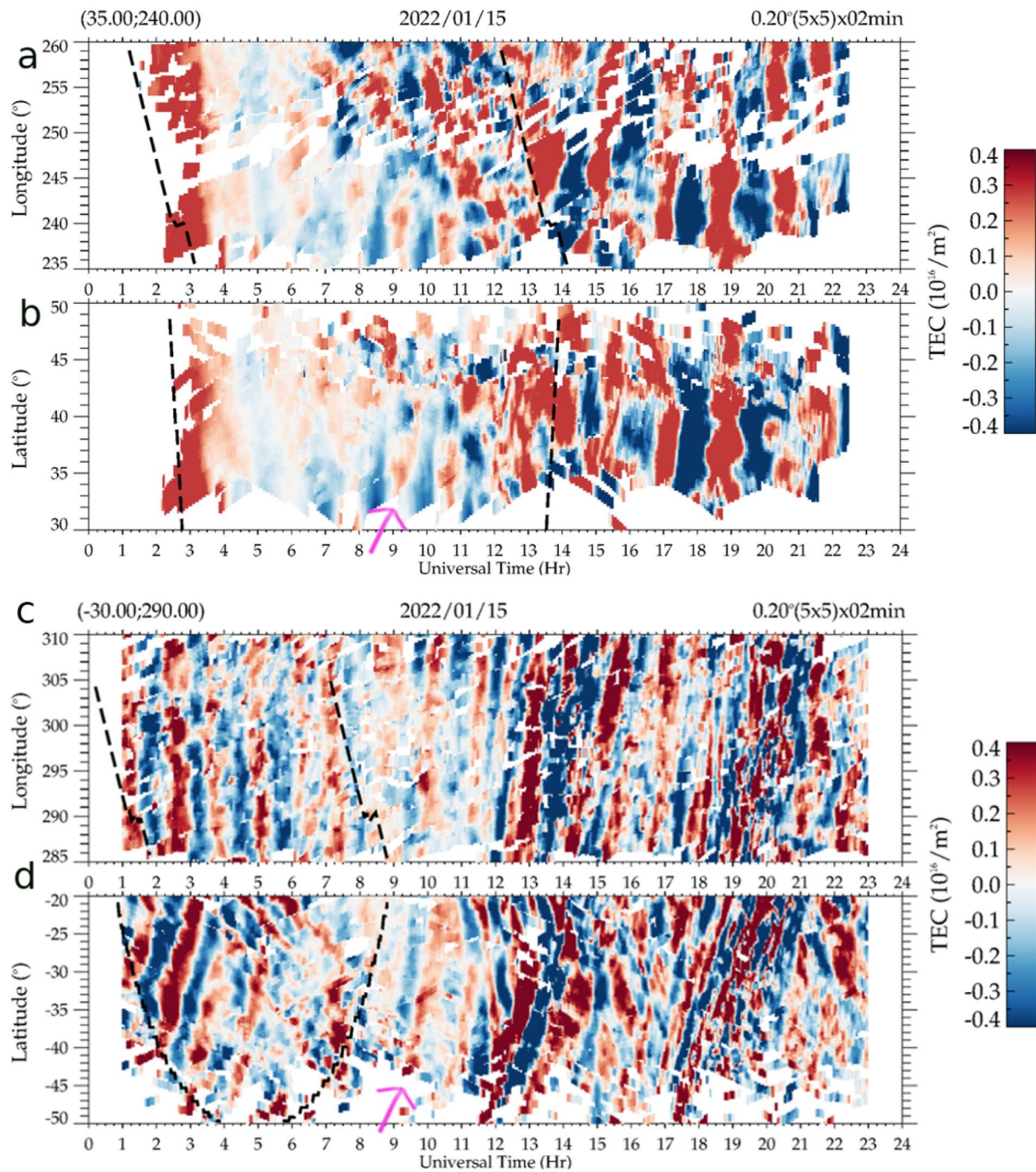


Figure 16. Keograms of the observed $vTEC$ over the western CONUS on 15 January 2022 at $35^{\circ}S$ (a) and $120^{\circ}W$ (b). Here we detrend with a 3 hr running mean. Keograms of the $vTEC$ over South America at $30^{\circ}S$ (c) and $70^{\circ}W$ (d). Here, we detrend with a 2 hr running mean. Purple arrows indicate the fastest LSTIDs from Tonga. Black dash lines show the sunrise and sunset terminators.

We now compare the ionosonde parameters with those from the SAMI3 Tonga run. In row 1, we show the foF2 from the SAMI3 Tonga run (solid line), and in row 2, we show the hmF2 from the SAMI3 Tonga run (solid lines) and the base run (dash lines). The LSTIDs are seen in the model results, although with amplitudes that are approximately 2 times smaller and at slightly later times. For example, the drop in the SAMI3 F peak is $\approx 50\text{--}90$ km and is delayed by ≈ 40 min as compared to the observations. This amplitude and timing difference is consistent with that of the neutral horizontal wind components of the secondary GWs as compared with the Tonga GWs observed by ICON-MIGHTI (Vadas, Becker, Figueiredo, et al., 2023).

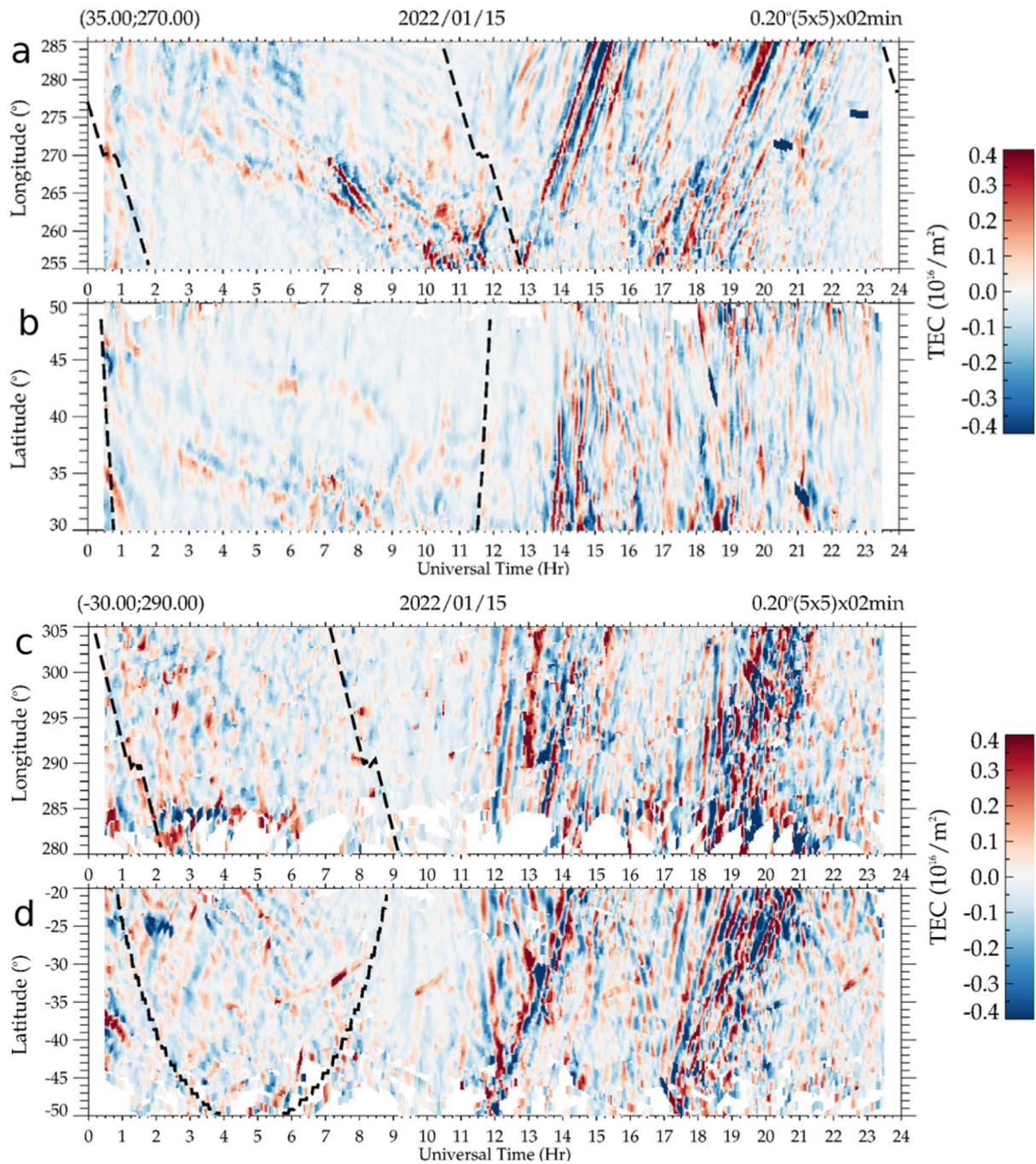


Figure 17. Keograms of the observed vTEC over the CONUS on 15 January 2022 at 35°N (a) and 90°W (b) and over South America at 30°S (c) and 70°W (d). We detrend with a 1 hr running mean. Black dash lines show the sunrise and sunset terminators.

6. Characteristics of the Lamb Waves Observed by AIRS

In this section, we more-precisely determine c_H and λ_H for the LWs observed by Wright et al. (2022) in the stratosphere. We use 4.3 μ brightness temperature observations from the AIRS instrument aboard NASA's Aqua satellite. The 4.3 μ channels peak near $z \simeq 40$ km with a vertical weighting function around 20 km deep (Hoffmann et al., 2014). Brightness temperatures are calculated for each measurement footprint in a 90-element wide across-track swath. These temperatures are then detrended using a fourth-order polynomial fit to reveal the perturbations, T' (Alexander & Barnett, 2007).

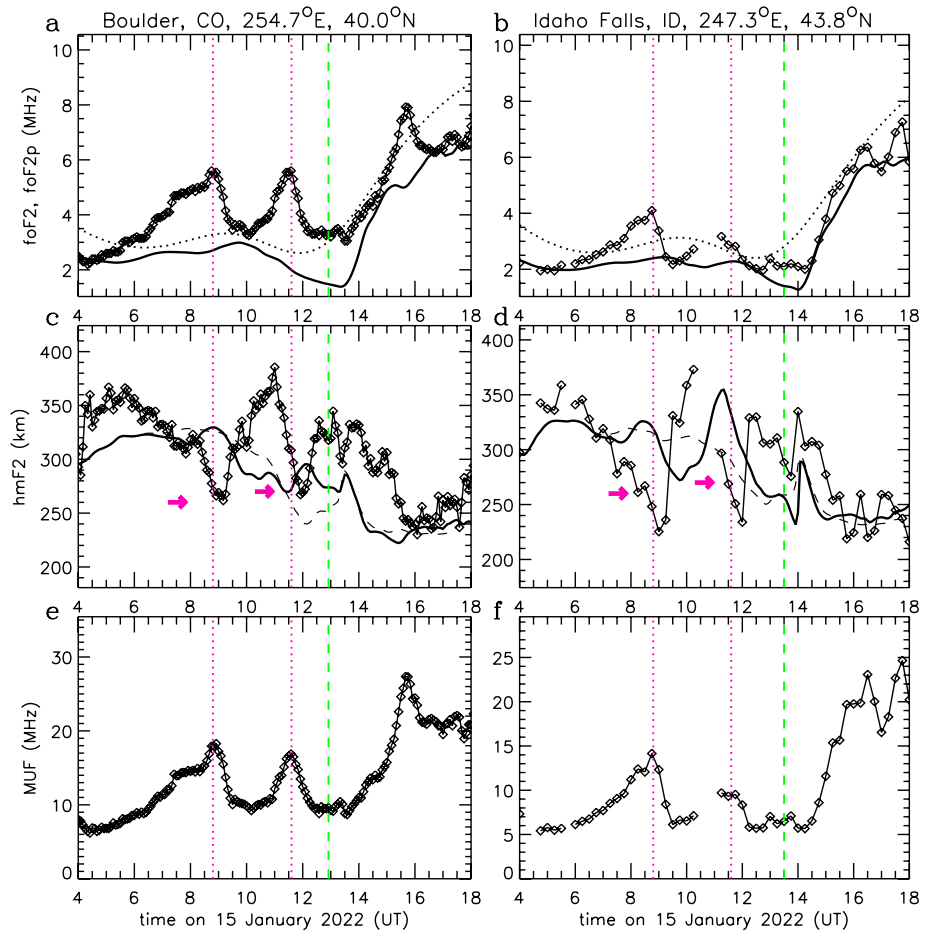


Figure 18. Parameters of ionosonde measurements on 15 January 2022 and comparison with SAMI3. (a) The manually scaled critical frequency of the F2 layer, foF2 (diamonds) at Boulder, Colorado (254.7°E and 40.0°N). The quiet-time International Reference Ionosphere URSI-option prediction, foF2p, is shown as the black dotted line. foF2 from the SAMI3 Tonga run is shown as the solid line. (b) The same as (a), but at Idaho Falls, ID (247.3°E and 43.8°N). (c)–(d) The same as row 1 but for the hmF2 (diamonds and solid line). The black dash line shows $\sqrt{\text{NmF2}/1.24}/100$ from the SAMI3 base run. Pink arrows point to the wave structure in hmF2. (e)–(f) The MUF, which is the Maximum Useable Frequency at a distance of 3,000 km (diamonds) at Boulder, CO and Idaho Falls, ID, respectively. The dotted pink lines show 8.8 and 11.6 UT. The green dash lines show the solar terminator at $z = 280$ km.

Figure 19a shows the AIRS T' south and southeast of Tonga at $\approx 11:20$ – $11:30$ UT on 15 January 2022. Concentric rings of LWs and GWs from the Tonga eruption are seen over Antarctica. Note that the LW consists of a single localized pulse (–+–), whereas the GW packet is quite broad and contains a long train of waves. Figures 19b and 19c show the AIRS T' as a function of distance R from Tonga. In addition, Figure 19b shows lines of constant horizontal phase speed of waves from Tonga, assuming an eruption time of 04:28:48 UT (as derived from surface pressure observations in Wright et al. (2022)). The LW is located at $R = 7,700$ – $8,100$ km from Tonga at this time. The leading edge of the LW has $c_H = 318.2 \pm 5.7$ m/s, which is well within the error bounds reported by Wright et al. (2022). Note that the leading edge of the primary GW packet is at $R = 6,300$ – $6,900$ and has speeds of $c_H = 250$ – 275 m/s. We roughly estimate $\lambda_H \approx 150$ km for the LW and $\lambda_H \approx 350$ – 400 km for the leading primary GWs from Figures 19b and 19c.

To obtain a more-precise measurement of λ_H for the LW, we interpolate T' in Figure 19c to a regular distance spacing, then apply the S-transform (Stockwell et al., 1996) using the method of Hindley et al. (2019). Figure 19d shows the result. The LW has a peak amplitude of ≈ 0.2 K at $\lambda_H = 146.058$ km. There is also a secondary LW peak at $\lambda_H \approx 290$ km. This superimposed characteristic is consistent with the visible T' for the LW in Figure 19a–19c. The total range of horizontal wavelengths for the LW is seen to be $\lambda_H = 70$ – 380 km. The LW with $\lambda_H = 380$ km has $T' \approx 0.1$ K and $\tau_r = \lambda_H/c_H \approx 20$ min.

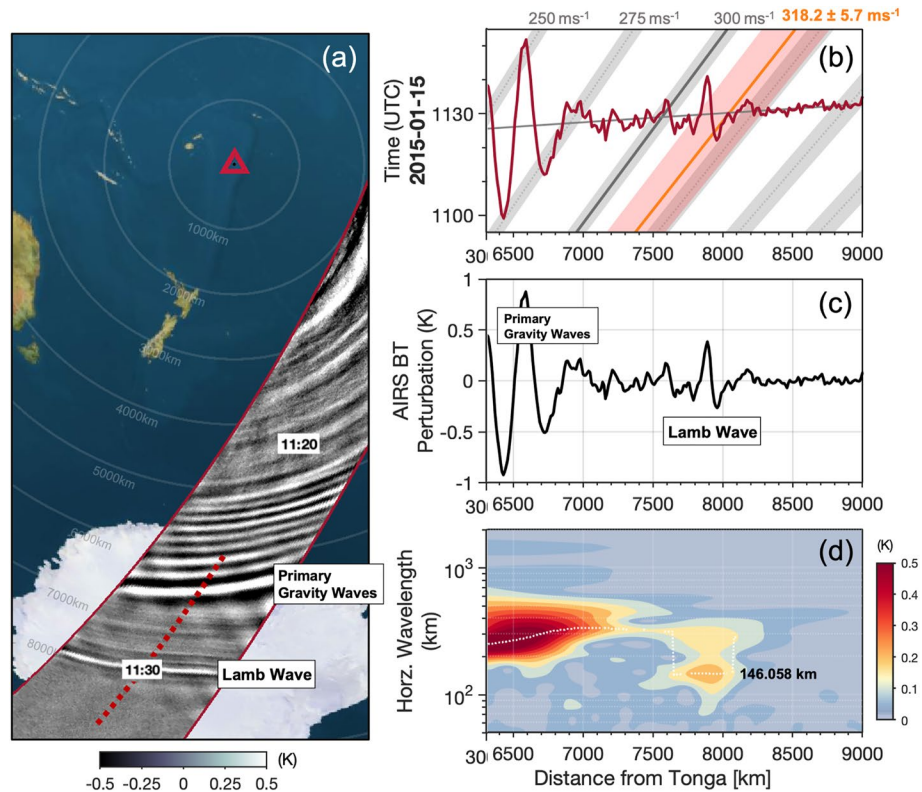


Figure 19. Lamb wave (LW) parameters determined from AIRS observations at $z \approx 40$ km on 15 January 2022. (a) 4.3μ brightness temperature perturbations, T' , (in K) for the AIRS overpass at 11:20–11:30 UTC. The red triangle shows Tonga and gray rings show the distance from Tonga, R , in 1,000 km intervals. (b)–(c) AIRS T' (in K, red and black lines, respectively) as functions of R along the red dash line in (a). T' is the same in (b)–(c). The amplitude of T' is shown on the y-axis in (c). In (b), gray diagonal lines show lines of constant phase speed for waves launched from Tonga at 04:28:48 UTC, and the orange lines and light orange shading show c_H with errors for the LW from Wright et al. (2022). (d) S-transform spectral analysis of the AIRS T' (in K). White dots indicate λ_H for the waves with the largest amplitudes at each R .

7. Conclusions

In this paper, we modeled the primary and secondary GWs and TIDs generated by the Hunga Tonga-Hunga Ha'apai volcanic eruption on 15 January 2022. We used MESORAC to excite, propagate and dissipate the primary GWs excited by the mechanical displacement of air from 4:15–5:50 UT, the HIAMCM to calculate the secondary GWs created where the primary GWs dissipated, and the SAMI3 to calculate the TIDs induced by the secondary GWs from the HIAMCM. We find that locally and globally-propagating MSTIDs and LSTIDs with concentric ring structure were induced by the secondary GWs through ion-neutral collisions. These TIDs had horizontal phase speeds of $c_H \approx 100$ –750 m/s, horizontal wavelengths of $\lambda_H \approx 600$ –6,000 km, and ground-based periods of $\tau_r \approx 30$ min to 3 hr. The LSTID distribution was found to be highly asymmetric because (a) the radiated secondary GW spectrum was highly asymmetric because the thermospheric body forces were meridionally-directed, thereby exciting negligible eastward and westward-propagating secondary GWs, and (b) the Earth's magnetic field \mathbf{B} is approximately northward near Tonga, thereby causing the zonally-propagating secondary GWs to induce TIDs with extremely small amplitudes. These two effects caused the amplitudes to be extremely small for the modeled LSTIDs over Australia and South Africa. The TID amplitudes were ≈ 2 –3 TECU near Tonga (over New Zealand), but decreased sharply $\approx 5,500$ km from Tonga (at the magnetic equator) because $\mathbf{v} \cdot \mathbf{B} \approx 0$ there. These model results agreed well with v TEC observations.

From the SAMI3 results, we found that the fastest TIDs from Tonga were LSTIDs, and reached the CONUS, South America, northern Europe and South Africa at $\sim 8:30$ UT, $\sim 9:00$ UT, $\sim 12:00$ UT, and $\sim 13:00$ UT, respectively, all with $c_H \approx 600$ m/s, $\lambda_H \approx 3,000$ –4,000 km and $\tau_r \approx 1.3$ –1.9 hr. They also reached Hawaii at 7:00 UT ($c_H \approx 700$ m/s, $\lambda_H \approx 2,200$ –2,400 km, $\tau_r \approx 55$ min), and Japan at 8:30 UT ($c_H \approx 600$ –650 m/s, $\lambda_H \approx 3,000$ –3,500 km,

and $\tau_r \simeq 1.3\text{--}1.6$ hr). We found that the fastest TIDs reached Australia at $\sim 7:30$ UT with much slower speeds of $c_H \simeq 400$ m/s. We found that the timing, speeds, and periods of the modeled TIDs agreed well with Themens et al. (2022).

From the SAMI3 results, we found that the MSTIDs followed the LSTIDs many hours later. For example, the MSTIDs reached the CONUS and South America at 12:00–16:00 UT, with $c_H \simeq 200\text{--}400$ m/s, $\lambda_H \simeq 600\text{--}1,000$ km, and $\tau_r \simeq 45\text{--}120$ min. We showed that the MSTIDs with the largest amplitudes over the CONUS had $c_H \simeq 200\text{--}300$ m/s.

We then analyzed the SAMI3 and observed TIDs using different detrend windows. We found that the first observed TIDs reached the CONUS at $\sim 8:30$ UT with $c_H = 682 \pm 100$ m/s, $\tau_r = 87 \pm 2$ min, and $\lambda_H = 3,560 \pm 604$ km, and reached South America at $\sim 9:00$ UT with $c_H = 675 \pm 58$ m/s, $\tau_r = 78 \pm 6$ min, and $\lambda_H = 3,159 \pm 514$ km using 3 and 2 hr detrend windows, respectively, in good agreement with the model results. We showed that the LSTIDs have extremely small amplitudes in the model results and vTEC data over the CONUS and South America if a 30 min detrend window is used instead because this window detrends out (eliminates) most TIDs with $\tau_r > 30$ min. This is why Zhang et al. (2022) did not observe these fast LSTIDs over the CONUS. As stated by Themens et al. (2022), “Use a detrending window that is too wide and you risk introducing substantial trends from quiescent ionospheric variability and masking smaller scale structures behind stronger large-scale variability. Use a detrending window that is too narrow and you risk removing parts of the desired signal...Using the 30-min window will allow us to easily identify the MSTIDs, but may artificially suppress the observed amplitude of LSTID structures”.

We found that the observed hmF2 drops by $\simeq 110\text{--}140$ km over Boulder, Colorado and Idaho Falls, ID with a 2.8 hr periodicity from 7:00 to 13:00 UT at the time when the fastest modeled LSTIDs from Tonga arrived there with $\tau_r \simeq 3$ hr. We found that the modeled results agreed well with the ionosonde data at $\sim 8:00\text{--}13:00$ UT over these locations provided we increased our modeled hmF2 changes by a factor of $\simeq 2$ and sampled our results $\simeq 40$ min later than the ionosonde. This adjustment is consistent with the comparison of the secondary GWs with the ICON-MIGHTI GWs from Tonga (Vadas, Becker, Figueiredo, et al., 2023), and is likely because the turbulent diffusion coefficient needed to be somewhat too large in MESORAC to keep the HIAMCM Tonga run from becoming unstable.

Finally, we more-precisely determined the parameters of the LWs observed by AIRS in the stratosphere (at $z \simeq 40$ km) by Wright et al. (2022), and found that the LWs had $\lambda_H = 70\text{--}380$ km, $c_H = 318.2 \pm 5.7$ m/s, and $T' = 0.1\text{--}0.2$ K. These values of λ_H are smaller than the far-field MSTIDs observed by Lin et al. (2022) and Zhang et al. (2022), which had $\lambda_H \simeq 400\text{--}2,000$ km. We reviewed the derivation of the LW solutions (Appendix A), and found that although the amplitude of a LW grows exponentially in altitude, it decays exponentially in altitude as compared to the amplitude of a GW. We found that the Tonga LW amplitude is $\simeq 2.3\%$ that of the primary GW at the assumed leakage altitude of $z \simeq 110$ km. Therefore, it is highly unlikely that the TIDs observed by Lin et al. (2022) and Zhang et al. (2022) were due to the leakage of the LWs into thermospheric GWs.

In conclusion, we found that the horizontal wavelengths, periods, and horizontal phase speeds of the observed TIDs from Tonga were fully explained by secondary GWs from Tonga, rather than by the leakage of stratospheric LWs into thermospheric GWs. Thus, secondary GWs from Tonga were important drivers of TIDs in the Earth's ionosphere during the Tonga event.

Appendix A: Lamb Wave Solution

In this appendix, we review the derivation of the LW solution in the atmosphere (Lamb, 1932). We start with the compressible, f-plane fluid equations. The momentum, mass and thermodynamic equations (for isentropic flow) are

$$\frac{D\mathbf{v}}{Dt} + \frac{1}{\rho} \nabla p - \mathbf{g} + 2\boldsymbol{\Omega} \times \mathbf{v} = 0, \quad (\text{A1})$$

$$\frac{D\rho}{Dt} + \rho \nabla \cdot \mathbf{v} = 0, \quad (\text{A2})$$

$$\frac{Dp}{Dt} + \gamma p \nabla \cdot \mathbf{v} = 0 \quad (\text{A3})$$

(e.g., Landau & Lifshitz, 1959], where $D/Dt = \partial/\partial t + (\mathbf{v} \cdot \nabla)$, $\mathbf{v} = (u, v, w)$, u , v , and w are the zonal, meridional, and vertical velocities, respectively, T is temperature, ρ is density, p is pressure, $\boldsymbol{\Omega}$ is Earth's rotation vector, and \mathbf{g} is the gravitational force. We use the ideal gas law, $p = r\rho T$, where $r = 8,308/X_{\text{MW}} \text{ m}^2 \text{ s}^{-2} \text{ K}^{-1}$, X_{MW} is the mean molecular weight of the particle in the gas, $\gamma - 1 = r/C_v$, and $\gamma = C_p/C_v$ is the ratio of specific heats, and C_p and C_v are the mean specific heats at constant pressure and volume, respectively. X_{MW} decreases from $X_{\text{MW}} = 28.9$ in the lower atmosphere to $X_{\text{MW}} = 16$ in the upper thermosphere, and γ correspondingly increases from $\gamma = 1.4$ to $\gamma = 1.67$ because of the change from diatomic to monatomic molecules, which occurs at $z \sim 150\text{--}300 \text{ km}$.

We expand the variables as background means (overlines) plus perturbations (primes):

$$\begin{aligned} u &= \bar{U} + u', & v &= \bar{V} + v', & w &= w' = 0, \\ \rho &= \bar{\rho} + \rho', & T &= \bar{T} + T', & p &= \bar{p} + p'. \end{aligned} \quad (\text{A4})$$

Here we have used the fact that the LW is characterized by zero vertical motion:

$$w' = 0. \quad (\text{A5})$$

We assume an isothermal atmosphere with constant temperature \bar{T} and constant background wind (\bar{U}, \bar{V}) . We neglect the Earth's curvature, which limits wave scales to $\lambda_H < 20,000\text{--}30,000 \text{ km}$. The f -plane approximation is $2\boldsymbol{\Omega} \times \mathbf{v}' \simeq f(-v'\hat{i} + u'\hat{j})$, where $f = 2\Omega \sin\phi$, ϕ is a fixed latitude, and f is fixed. The vertical momentum equation reduces to the hydrostatic equation, $d\bar{p}/dz = -g\bar{\rho}$, yielding

$$\bar{\rho} = \bar{\rho}_0 e^{-z/H}, \quad \bar{p} = \bar{p}_0 e^{-z/H}, \quad (\text{A6})$$

where $H = -\bar{\rho}(d\bar{p}/dz)^{-1} = r\bar{T}_0/g$ is the density scale height, and $\bar{\rho}_0$, \bar{T}_0 , and \bar{p}_0 are the mean density, temperature, and pressure at $z = 0$, respectively. Linearizing Equations A1–A3, we obtain

$$\frac{d\mathbf{v}'}{dt'} + \frac{1}{\bar{\rho}} \nabla p' - \frac{\rho'}{\bar{\rho}^2} \nabla \bar{p} + f(-v'\hat{i} + u'\hat{j}) = 0, \quad (\text{A7})$$

$$\frac{d\rho'}{dt'} + (\mathbf{v}' \cdot \nabla) \bar{\rho} + \bar{\rho} \nabla \cdot \mathbf{v}' = 0, \quad (\text{A8})$$

$$\frac{dp'}{dt'} + \mathbf{v}' \cdot \nabla \bar{p} + \gamma \bar{p} \nabla \cdot \mathbf{v}' = 0, \quad (\text{A9})$$

where $d/dt' = (\partial/\partial t + \bar{U}\partial/\partial x + \bar{V}\partial/\partial y)$. We define

$$\begin{aligned} \hat{u} &= e^{-\alpha z} u', & \hat{v} &= e^{-\alpha z} v', \\ \hat{\rho} &= e^{-\alpha z} \rho' / \bar{\rho}, & \hat{p} &= e^{-\alpha z} p' / \bar{p}, & \hat{T} &= e^{-\alpha z} T' / \bar{T}_0, \end{aligned} \quad (\text{A10})$$

where α is a constant that will be determined as part of the solution. We expand all “hatted” variables as:

$$\hat{u} = \hat{u}_0 e^{i(\omega_r t - kx - ly)}, \quad (\text{A11})$$

where k and l are the zonal and meridional wavenumbers and ω_r is the observed frequency. Note that $p'/\bar{p} = \rho'/\bar{\rho} + T'/\bar{T}$ from the ideal gas law, which leads to

$$\hat{T} = \frac{\gamma}{c_s^2} \hat{p} - \hat{\rho}. \quad (\text{A12})$$

When solving Equations A7–A9 with these definitions, we find that the exponential growth factor for a LW is

$$\alpha = \frac{1}{H} - \frac{g}{c_s^2} = \frac{1}{H} - \frac{1}{\gamma H} = \frac{\gamma - 1}{\gamma H}, \quad (\text{A13})$$

and that the LW dispersion relation is

$$\omega_{I_r}^2 = f^2 + c_s^2 k_H^2, \quad (\text{A14})$$

where $k_H^2 = k^2 + l^2$ and the intrinsic frequency is

$$\omega_{I_r} = \omega_r - (k\bar{U} + l\bar{V}). \quad (\text{A15})$$

The LW polarization relations are

$$\hat{u}_0 = \frac{ik\omega_{I_r} + fl}{il\omega_{I_r} - fk} \hat{v}_0, \quad (\text{A16})$$

$$\hat{p}_0 = c_s^2 \hat{\rho}_0, \quad (\text{A17})$$

$$\hat{\rho}_0 = \frac{ik_H^2}{ik\omega_{I_r} + fl} \hat{u}_0, \quad (\text{A18})$$

$$\hat{T}_0 = (\gamma - 1)\hat{p}_0, \quad (\text{A19})$$

where the sound speed, c_s , is defined via

$$c_s^2 = \gamma g \mathcal{H} = \gamma r \bar{T}_0 = \gamma \bar{p}_0 / \bar{\rho}_0. \quad (\text{A20})$$

If the assumed oscillatory form of the LW is $e^{i(-\omega_r t + kx + ly)}$ instead of Equation A11, we replace i by $-i$ in Equations A16–A19. From Equation A14, the horizontal phase speed of a LW is c_s if $c_s^2 k_H^2 \gg f^2$. Note that for a LW,

$$\rho' = \rho'(z_i) \exp[-g(z - z_i)/c_s^2], \quad (\text{A21})$$

where z_i is the reference altitude, in agreement with previous results (e.g., Otsuka, 2022; Garrett, 1969).

Although the amplitude of a LW grows exponentially in altitude, it does not grow as rapidly in z as do the amplitudes of GWs and AWs, which grow as $\exp(z/2\mathcal{H})$ in the absence of Doppler shifting and dissipation (Hines, 1960). This can be seen from rewriting Equation A13 as

$$\alpha = \frac{1}{2\mathcal{H}} + \frac{\gamma - 2}{2\gamma\mathcal{H}}, \quad (\text{A22})$$

and noting that $(\gamma - 2)/(2\gamma\mathcal{H})$ is negative at all altitudes (since $\gamma = 1.4$ to 1.667). Therefore, if a LW and a GW have amplitudes of $T'_{LW}(z_i)$ and $T'_{GW}(z_i)$ at $z = z_i$, respectively, the amplitude ratio at a higher altitude z is

$$\frac{T'_{LW}(z)}{T'_{GW}(z)} = \frac{T'_{LW}(z_i)}{T'_{GW}(z_i)} \exp\left(-\frac{(2 - \gamma)(z - z_i)}{2\gamma\mathcal{H}}\right). \quad (\text{A23})$$

Thus, the increase of a LW's amplitude with height is exponentially smaller than that of a GW or an AW; *the amplitude of a LW decreases exponentially in altitude as compared to the amplitude of a GW or AW*. For an atmosphere with diatomic molecules, $2\gamma\mathcal{H}/(2 - \gamma) = 4.7\mathcal{H}$.

Even with a relatively small amplitude, a LW can still force/excite (i.e., leak) GWs in the lower thermosphere at and above the altitude where $310 \text{ m/s} \approx 0.9c_s$ or $c_s \approx 344 \text{ m/s}$. From Figure 2b of Vadas (2007), this is estimated to occur at $z \approx 110 \text{ km}$. If a LW packet is broad spatially and contains many oscillations, then the excited GW will have the same ω_r and k_H as that of the LW. A localized LW packet, however, is expected to not only excite GWs at this fundamental frequency, but also at several discrete frequencies and at a continuum of frequencies as well (although with smaller amplitudes); this is similar to that of a tsunami, which excites discrete GWs and a continuum of GWs in addition to the GWs at the fundamental frequency (Vadas et al., 2015). We ignore the complication of a localized LW packet exciting a spectrum of GWs here, because it will not affect our amplitude ratio argument.

We now investigate the Tonga LWs observed by AIRS. We consider the LW from Figure 19d with $\lambda_H = 380 \text{ km}$ and $\tau_r = 20 \text{ min}$, which would avoid being trapped in the lower thermosphere (see Section 1). This LW has $T'_{LW}(z_i) \approx 0.1 \text{ K}$ from Figures 19b–19d, where $z_i \approx 40 \text{ km}$. The leading edge of the primary GWs have

$T'_{GW}(z_i) \approx 0.5$ K from Figures 19b–19d. Therefore, the ratio of their amplitudes at the estimated leakage altitude of $z \approx 110$ km is estimated to be

$$\frac{T'_{LW}}{T'_{GW}} \approx \frac{0.1}{0.5} \exp\left(-\frac{(2-\gamma)(z-z_i)}{2\gamma H}\right) \approx 0.023 \quad (\text{A24})$$

from Equation A23, where we have set $\gamma = 1.4$ and $H = 7$ km. Thus the LW amplitude at the leakage altitude is only $\approx 2.3\%$ that of the primary GW amplitudes there. The primary GWs break and dissipate near or above the leakage altitude, thereby creating secondary GWs. The secondary GW amplitudes are 5–10 smaller than those of the primary GWs at the excitation altitude (e.g., Vadas et al., 2018). Thus we estimate that the amplitudes of the thermospheric GWs forced by the LWs would be 4–9 times smaller than that of the secondary GWs. Therefore, it is very unlikely that the leakage of LWs into thermospheric GWs plays a significant role in the F region TIDs from Tonga as compared to the role that the secondary GWs play there.

Data Availability Statement

MERRA-2 reanalysis data was used to nudge the HIAMCM, and is available in English for download at https://gmao.gsfc.nasa.gov/reanalysis/MERRA-2/data_access/. The Global Navigation Satellite System (GNSS) RINEX files used in this work are available from the Geological hazard information for New Zealand at <https://www.geonet.org.nz/data/types/geodetic>, the Geoscience Australia GNSS data archive at <https://www.ga.gov.au/scientific-topics/positioning-navigation/geodesy/gnss-networks>, Instituto Brasileiro de Geografia e Estatística (RMBC) <https://www.ibge.gov.br/geociencias/informacoes-sobre-posicionamento-geodesico/rede-geodesica/>, NOAA Continuously Operating Reference Stations (CORS) Network at <https://geodesy.noaa.gov/CORS/data.shtml>, Centro Sismológico Nacional at <https://gps.csn.uchile.cl>, and Red Argentina de Monitoreo Satelital Continuo (RAMSAC) at <https://www.ign.gob.ar/NuestrasActividades/Geodesia/Ramsac/DescargaRinex>. The ionogram data used to make Figure 18 can be downloaded in English from Lowell DIDBase (didbase.giro.uml.edu) or <https://giro.uml.edu>. The ionogram data was processed manually using the SAOExplorer tool (available at the same website). High-rate GPS data from Hawaii is publicly available via UNAVCO database (<https://data.unavco.org/archive/>). The model data shown in this paper will be available in English at the time of publication at <https://www.cora.nwra.com/vadas/Vadas-et-al-JGR-2023-TongaTEC-files/>.

Acknowledgments

We would like to thank two anonymous reviewers for helpful comments. SLV and EB were supported by NSF Grant AGS-1832988 and NASA Grants 80NSSC20K0628 and 80NSSC19K0836, and 80NSSC22K0174. CF was supported by Fundação de Amparo à Pesquisa do Estado de São Paulo (FAPESP) under the Grants 2018/09066-8 and 2019/22548-4. JDH was supported by NASA Grants 80NSSC22K0174 and 80NSSC21K1305, and AFOSR Grant F4FGA01252A005. DT's contribution to this study was supported through Canadian Space Agency Grant 21SUSTCHAI and Natural Environment Research Council grant NE/W003368/1. NPH was supported by UK NERC Grant NE/S00985X/1. SM acknowledges support from NASA 80NSSC21K1321, 80GSFC22CA011, and the International Space Science Institute (ISSI) in Bern and Beijing, through ISSI International Team project #511 (Multi-Scale Magnetosphere-Ionosphere-Thermosphere Interaction). IG was supported by UML GAMBIT Situation Room 2022 subscription fees. The Boulder Digisonde data are courtesy of NOAA/NCEI Ionosonde Group, station manager is Dr. Terence Bullett. The Idaho Falls Digisonde data are courtesy of Idaho National Laboratory, station manager is Dr. James Hanneman. KB was supported by NASA Grant 80NSSC19K0836. We would like to thank the NASA HECC and the Leibniz Institute of Atmospheric Physics at the University of Rostock (IAP) for providing the HPC facilities used for this study.

References

- Alexander, M. J., & Barnett, C. (2007). Using satellite observations to constrain parameterizations of gravity wave effects for global models. *Journal of the Atmospheric Sciences*, 64(5), 1652–1665. <https://doi.org/10.1175/jas3897.1>
- Altadill, D., Segarra, A., Blanch, E., Juan, J. M., Paznukhov, V. V., Buresova, D., et al. (2020). A method for real-time identification and tracking of traveling ionospheric disturbances using ionosonde data: First results. *Journal of Space Weather and Space Climate*, 10, 2. <https://doi.org/10.1051/swsc/2019042>
- Amores, A., Monserrat, S., Marcos, M., Argüeso, D., Villalonga, J., Jordà, G., & Gomis, D. (2022). Numerical simulation of atmospheric Lamb waves generated by the 2022 Hunga-Tonga volcanic eruption. *Geophysical Research Letters*, 49(6), e2022GL098240. <https://doi.org/10.1029/2022GL098240>
- Aryal, S., Geddes, G., Finn, S. C., Mrak, S., Galkin, I., Cnossen, I., et al. (2019). Multispectral and multi-instrument observation of TIDs following the total solar eclipse of 21 August 2017. *Journal of Geophysical Research: Space Physics*, 124(5), 3761–3774. <https://doi.org/10.1029/2018JA026333>
- Astafeyeva, E., Maletkii, B., Mikesell, T. D., Munaibari, E., Ravanelli, M., Coisson, P., et al. (2022). The 15 January 2022 Hunga Tonga eruption history as inferred from ionospheric observations. *Geophysical Research Letters*, 49(10), e2022GL098827. <https://doi.org/10.1029/2022GL098827>
- Becker, E., Goncharenko, L., Harvey, V. L., & Vadas, S. L. (2022). Multi-step vertical coupling during the January 2017 sudden stratospheric warming. *Journal of Geophysical Research: Space Physics*, 127(12), e2022JA030866. <https://doi.org/10.1029/2022JA030866>
- Becker, E., & Vadas, S. L. (2020). Explicit global simulation of gravity waves in the thermosphere. *Journal of Geophysical Research: Space Physics*, 125(10). <https://doi.org/10.1029/2020JA028034>
- Becker, E., Vadas, S. L., Bossert, K., Harvey, V. L., Züllicke, C., & Hoffmann, L. (2022). A high-resolution whole-atmosphere model with resolved gravity waves and specified large-scale dynamics in the troposphere and stratosphere. *Journal of Geophysical Research: Space Physics*, 127(2), e2021JD035018. <https://doi.org/10.1029/2021JD035018>
- Figueiredo, C., Wrasse, C. M., Takahashi, H., Otsuka, Y., Shiokawa, K., & Barros, D. (2017). Large-scale traveling ionospheric disturbances observed by GPS dTEC maps over North and South America on Saint Patrick's Day storm in 2015. *Journal of Geophysical Research: Space Physics*, 122(4), 4755–4763. <https://doi.org/10.1002/2016JA023417>
- Garrett, C. J. R. (1969). Atmospheric edge waves. *Quarterly Journal of the Royal Meteorological Society*, 95(406), 731–753. <https://doi.org/10.1002/qj.49709540607>
- Hain, K. (1987). The partial donor cell method. *Journal of Computational Physics*, 73(1), 131–147. [https://doi.org/10.1016/0021-9991\(87\)90110-0](https://doi.org/10.1016/0021-9991(87)90110-0)
- Harding, B. J., Wu, Y.-J. J., Alken, P., Yamazaki, Y., Triplett, C. C., Immel, T. J., et al. (2022). Impacts of the January 2022 Tonga volcanic eruption on the ionospheric dynamo: ICON-MIGHTI and Swarm observations of extreme neutral winds and currents. *Geophysical Research Letters*, 49(9), e2022GL098577. <https://doi.org/10.1029/2022GL098577>

- Heale, C. J., Bossert, K., Vadas, S., Hoffmann, L., Dornbrack, A., Stober, G., et al. (2020). Secondary gravity waves generated by breaking mountain waves over Europe. *Journal of Geophysical Research: Atmospheres*, *125*(5). <https://doi.org/10.1029/2019JD031662>
- Heki, K. (2022). Ionospheric signatures of repeated passages of atmospheric waves by the 2022 Jan. 15 Hunga Tonga-Hunga Ha'apai eruption detected by QZSS-TEC observations in Japan. *Earth Planets and Space*, *74*(1), 112. <https://doi.org/10.1186/s40623-022-01674-7>
- Hindley, N. P., Wright, C. J., Smith, N. D., Hoffmann, L., Holt, L. A., Alexander, M. J., et al. (2019). Gravity waves in the winter stratosphere over the southern ocean: High-resolution satellite observations and 3-D spectral analysis. *Atmospheric Chemistry and Physics*, *19*(15), 15377–15414. <https://doi.org/10.5194/acp-19-15377-2019>
- Hines, C. O. (1960). Internal atmospheric gravity waves at ionospheric heights. *Canadian Journal of Physics*, *38*(11), 1441–1481. <https://doi.org/10.1139/p60-150>
- Hoffmann, L., Alexander, M. J., Clerbaux, C., Grimsdell, A. W., Meyer, C. I., Robler, T., & Tournier, B. (2014). Intercomparison of stratospheric gravity wave observations with AIRS and IASI. *Atmospheric Measurement Techniques*, *7*(12), 4517–4537. <https://doi.org/10.5194/amt-7-4517-2014>
- Huba, J., & Joyce, G. (2010). Global modeling of equatorial plasma bubbles. *Geophysical Research Letters*, *37*(17), L17104. <https://doi.org/10.1029/2010GL044281>
- Huba, J., Joyce, G., & Fedder, J. (2000). Sami2 (Sami2 is another model of the ionosphere): A new low-latitude ionosphere model. *Journal of Geophysical Research*, *105*, 23035. <https://doi.org/10.1029/2010GL044281>
- Huba, J. D. (2003). A tutorial on hall magnetohydrodynamics. In M. Scholer, C. T. Dum, & J. Buchner (Eds.), *Space simulations* (p. 170). Springer.
- Huba, J. D., Becker, E., & Vadas, S. L. (2023). Simulation study of the 15 January 2022 Tonga event: Development of super equatorial plasma bubbles. *Geophysical Research Letters*, *50*(1), e2022GL101185. <https://doi.org/10.1029/2022GL101185>
- Huba, J. D., Drob, D. P., Wu, T.-W., & Makela, J. J. (2015). Modeling the ionospheric impact of tsunami-driven gravity waves with SAMI3: Conjugate effects. *Geophysical Research Letters*, *42*(14), 5719–5726. <https://doi.org/10.1002/2015GL064871>
- Huba, J. D., & Liu, H.-L. (2020). Global modeling of equatorial spread F with SAMI3/WACCM-X. *Geophysical Research Letters*, *47*(14). <https://doi.org/10.1029/2020GL088258>
- Krall, J., Huba, J. D., & Fritts, D. C. (2013). On the seeding of equatorial spread F by gravity waves. *Geophysical Research Letters*, *40*(4), 661–664. <https://doi.org/10.1002/GRL.50144>
- Lamb, H. (1932). *Hydrodynamics*. Cambridge University Press.
- Landau, L., & Lifshitz, E. (1959). *Fluid mechanics*. (pp. 536). Pergamon Press.
- Li, R., Lei, J., Kusche, J., Dang, T., Huang, F., Luan, X., et al. (2023). Large-scale disturbances in the upper thermosphere induced by the 2022 Tonga volcanic eruption. *Geophysical Research Letters*, *50*(3), e2022GL102265. <https://doi.org/10.1029/2022GL102265>
- Lin, J.-T., Rajesh, P. K., Lin, C. C. H., Chou, M.-Y., Liu, J.-Y., Yue, J., et al. (2022). Rapid conjugate appearance of the giant ionospheric Lamb wave signatures in the Northern hemisphere after Hunga-Tonga volcano eruptions. *Geophysical Research Letters*, *49*(8), e2022GL098222. <https://doi.org/10.1029/2022GL098222>
- Matoza, R. S., Fee, D., Assink, J. D., Iezzi, A. M., Green, D. N., Kim, K., et al. (2022). Atmospheric waves and global seismoacoustic observations of the January 2022 Hunga eruption, Tonga. *Science*, *377*(6601), 95–100. <https://doi.org/10.1126/science.aba7063>
- Mrak, S., Semeter, J., Nishimura, Y., & Coster, A. J. (2021). Extreme low-latitude total electron content enhancement and global positioning system scintillation at dawn. *Space Weather*, *19*(9). <https://doi.org/10.1029/2021SW002740>
- Mrak, S., Semeter, J., Nishimura, Y., Rodrigues, F. S., Coster, A. J., & Groves, K. (2020). Leveraging geodetic GPS receivers for ionospheric scintillation science. *Radio Science*, *55*(11), 1–17. <https://doi.org/10.1029/2020RS007131>
- Nicolls, M. J., Vadas, S. L., Aponte, N., & Sulzer, M. P. (2014). Horizontal wave parameters of daytime thermospheric gravity waves and E-region neutral winds over Puerto Rico. *Journal of Geophysical Research*, *119*(1), 576–600. <https://doi.org/10.1002/2013JA018988>
- Nishida, K., Kobayashi, N., & Fukao, Y. (2014). Background Lamb waves in the Earth's atmosphere. *Geophysical Journal International*, *196*(1), 312–316. <https://doi.org/10.1093/gji/ggt413>
- Otsuka, S. (2022). Visualizing Lamb waves from a volcanic eruption using meteorological satellite Himawari-8. *Geophysical Research Letters*, *49*(8), e2022GL098324. <https://doi.org/10.1029/2022GL098324>
- Reinisch, B. W., & Galkin, I. A. (2011). Global ionospheric radio observatory (GIRO). *Earth Planets and Space*, *63*(4), 377–381. <https://doi.org/10.5047/eps.2011.03.001>
- Shinbori, A., Otsuka, Y., Sori, T., Nishioka, M., Perwitasari, S., Tsuda, T., & Nishitani, N. (2022). Electromagnetic conjugacy of ionospheric disturbances after the 2022 Hunga Tonga-Hunga Ha'apai volcanic eruption as seen in GNSS-TEC and SuperDARN Hokkaido pair of radars observations. *Earth Planets and Space*, *74*(1), 106. <https://doi.org/10.1186/s40623-022-01665-8>
- Stockwell, R. G., Mansinha, L., & Lowe, R. P. (1996). Localization of the complex spectrum: The S-transform. *IEEE Transactions on Signal Processing*, *44*(4), 998–1001. <https://doi.org/10.1109/78.492555>
- Themens, D. R., Watson, C., Zagar, N., Vasylyevych, S., Elvidge, S., McCaffrey, A., et al. (2022). Global propagation of ionospheric disturbances associated with the 2022 Tonga volcanic eruption. *Geophysical Research Letters*, *49*(7), e2022GL098158. <https://doi.org/10.1029/2022GL098158>
- Tsugawa, T., Otsuka, Y., Coster, A. J., & Saito, A. (2007). Medium-scale traveling ionospheric disturbances detected with dense and wide TEC maps over North America. *Geophysical Research Letters*, *34*(22), L22101. <https://doi.org/10.1029/2007GL031663>
- Vadas, S., Yue, J., & Nakamura, T. (2012). Mesospheric concentric gravity waves generated by multiple convection storms over the North America Great Plain. *Journal of Geophysical Research*, *117*, D07113. <https://doi.org/10.1029/2011JD017025>
- Vadas, S. L. (2007). Horizontal and vertical propagation and dissipation of gravity waves in the thermosphere from lower atmospheric and thermospheric sources. *Journal of Geophysical Research*, *112*(A6), A06305. <https://doi.org/10.1029/2006JA011845>
- Vadas, S. L. (2013). Compressible *f*-plane solutions to body forces, heatings, and coolings, and application to the primary and secondary gravity waves generated by a deep convective plume. *Journal of Geophysical Research: Space Physics*, *118*(5), 2377–2397. <https://doi.org/10.1002/jgra.50163>
- Vadas, S. L., & Azeem, I. (2021). Concentric secondary gravity waves in the thermosphere and ionosphere over the continental United States on 25–26 March 2015 from deep convection. *Journal of Geophysical Research: Space Physics*, *126*(2), e2020JA028275. <https://doi.org/10.1029/2020JA028275>
- Vadas, S. L., & Becker, E. (2019). Numerical modeling of the generation of tertiary gravity waves in the mesosphere and thermosphere during strong mountain wave events over the Southern Andes. *Journal of Geophysical Research: Space Physics*, *124*(9), 7687–7718. <https://doi.org/10.1029/2019JA026694>

- Vadas, S. L., Becker, E., Bossert, K., Baumgarten, G., Hoffmann, L., & Harvey, V. L. (2023). Secondary gravity waves from the stratospheric polar vortex over ALOMAR Observatory on 12–14 January. *Journal of Geophysical Research: Atmospheres*, *128*(2), e2022JD036985. <https://doi.org/10.1029/2022JD036985>
- Vadas, S. L., Becker, E., Figueiredo, C., Bossert, K., Harding, B., & Gasque, C. (2023). Primary and secondary gravity waves and global wind changes generated by the Tonga volcanic eruption on 15 January 2022: Modeling and comparison with ICON-MIGHTI winds. *Journal of Geophysical Research: Space Physics*, *128*(2), e2022JA031138. <https://doi.org/10.1029/2022JA031138>
- Vadas, S. L., & Fritts, D. C. (2005). Thermospheric responses to gravity waves: Influences of increasing viscosity and thermal diffusivity. *Journal of Geophysical Research*, *110*(D15), D15103. <https://doi.org/10.1029/2004JD005574>
- Vadas, S. L., & Fritts, D. C. (2009). Reconstruction of the gravity wave field from convective plumes via ray tracing. *Annales Geophysicae*, *27*(1), 147–177. <https://doi.org/10.5194/angeo-27-147-2009>
- Vadas, S. L., Fritts, D. C., & Alexander, M. J. (2003). Mechanism for the generation of secondary waves in wave breaking regions. *Journal of the Atmospheric Sciences*, *60*(1), 194–214. <https://doi.org/10.1029/2004JD005574>
- Vadas, S. L., Makela, J. J., Nicolls, M. J., & Milliff, R. F. (2015). Excitation of gravity waves by ocean surface wave packets: Upward propagation and reconstruction of the thermospheric gravity wave field. *Journal of Geophysical Research*, *120*(11), 9748–9780. <https://doi.org/10.1002/2015JA021430>
- Vadas, S. L., Xu, S., Yue, J., Bossert, K., Becker, E., & Baumgarten, G. (2019). Characteristics of the quiet-time hotspot gravity waves observed by GOCE over the Southern Andes on 5 July 2010. *Journal of Geophysical Research: Space Physics*, *124*(8), 7034–7061. <https://doi.org/10.1029/2019JA026693>
- Vadas, S. L., Yue, J., She, C.-Y., Stamus, P., & Liu, A. (2009). A model study of the effects of winds on concentric rings of gravity waves from a convective plume near Fort Collins on 11 May 2004. *Journal of Geophysical Research*, *114*(D6), D06103. <https://doi.org/10.1029/2008JD010753>
- Vadas, S. L., Zhao, J., Chu, X., & Becker, E. (2018). The excitation of secondary gravity waves from local body forces: Theory and observation. *Journal of Geophysical Research: Atmospheres*, *123*(17), 9296–9325. <https://doi.org/10.1029/2017JD027970>
- Verhulst, T. G. W., Altadill, D., Barta, V., Belehaki, A., Buresová, D., Cesaroni, C., et al. (2022). Multi-instrument detection in Europe of ionospheric disturbances caused by the 15 January 2022 eruption of the Hunga volcano. *Journal of Space Weather and Space Climate*, *12*, 35. <https://doi.org/10.1051/swsc/2022032>
- Wright, C. J., Hindley, N. P., Alexander, M. J., Barlow, M., Hoffmann, L., Mitchell, C. N., et al. (2022). Surface-to-space atmospheric waves from Hunga Tonga-Hunga Ha'apai eruption. *Nature*, *609*(7928), 741–746. <https://doi.org/10.1038/s41586-022-05012-5>
- Yue, J., Vadas, S. L., She, C.-Y., Nakamura, T., Reising, S. C., Liu, H.-L., et al. (2009). Concentric gravity waves in the mesosphere generated by deep convective plumes in the lower atmosphere near Fort Collins. *Journal of Geophysical Research*, *114*(D6), D06104. <https://doi.org/10.1029/2008JD011244>
- Zhang, S.-R., Vierinen, J., Aa, E., Goncharenko, L., Erickson, P., Rideout, W., et al. (2022). Tonga volcanic eruption induced global propagation of ionospheric disturbances via Lamb waves. *Frontiers in Astronomy and Space Sciences*, *9*. <https://doi.org/10.3389/fspas.2022.871275>